J. Fluid Mech. (1981), *vol.* 111, *pp.* 367–409
Printed in Great Britain

The interaction of long and short internal gravity waves: theory and experiment

By C. G. KOOP AND L. G. REDEKOPP†

Fluid Mechanics Department, TRW Systems, One Space Park,
Redondo Beach, CA 90278

(Received 7 August 1980 and in revised form 9 January 1981)

An analysis is presented which describes the slow-time evolution of an internal gravity wave in an arbitrarily specified stratification. The weakly nonlinear description of a single-wave mode, governed by the nonlinear Schrödinger equation, breaks down when certain resonant conditions are satisfied. One such condition occurs when the group velocity of the wavetrain is equal to the phase velocity of a higher-mode long wave of the system. The resonant interaction occurs on a faster time scale and is described by a coupled pair of nonlinear partial differential equations governing the evolution of both the short-wave and the long-wave modes. This long-wave/short-wave interaction is pursued further in an experimental investigation by measuring the modal interchange of energy between two internal waves of disparate length and time scales. The resulting data are compared with numerical solutions of the long-wave/short-wave resonant interaction equations. In general, the agreement between the theory and the experiment is reasonably good in the range of operating conditions for which the theory is valid.

1. Introduction

An important aspect of internal wave motions in the oceanic environment is the coupling which exists between motions occurring on widely different scales. It is generally felt that some of the weak background shearing motions associated with short vertical coherence scales are intimately connected to the propagating wavefield, as discussed by McIntyre (1973). The present work is directed toward gaining some understanding of such an interaction by addressing the problem of a nonlinear interaction between two narrow-band internal-wave modes with disparate length and time scales.

Grimshaw (1977) studied the weakly nonlinear evolution of a single internal wave mode and noted that the theory failed when the group velocity of the given mode coincided with the long-wave phase velocity of a higher mode. In this situation, a resonance occurs between the two wave modes and the problem must be reformulated on a faster time scale than was initially assumed. This same resonance mechanism was studied earlier by Djordjevic & Redekopp (1977) in the context of free-surface capillary–gravity waves and the appropriate evolution equations describing the long-time interaction were derived. In the internal-wave case, the long-wave/short-wave resonance provides a strong mechanism for dynamic coupling between the

---

† Permanent address: Department of Aerospace Engineering, University of Southern California, Los Angeles.

low-mode short waves and the weak shearing motions associated with long waves of low vertical coherence which are quite prevalent in the ocean (cf. Pinkel 1975).

The theoretical background for the derivation of the coupled evolution equations is reviewed in §2 in order to establish the context of the interaction and to emphasize several aspects of internal-wave motions in structured thermoclines. Calculations for a specific model are presented to demonstrate the prominence of these resonances and to reveal their spectral bandwidth and density. We also present a linearized stability analysis together with numerical simulations of the evolution system to understand both the short- and long-time dynamics of the resonant interaction. The present study focuses on the interaction of wavetrains and does not deal with some of the interesting solitary wave solutions of the equations which are discussed separately by Ma & Redekopp (1979).

Because of the potential importance of this resonance phenomenon in a number of dispersive wave systems, we have chosen to supplement the analytical work with an experimental investigation. The configuration chosen consists of three mutually immiscible homogeneous layers with different densities. Each of the two internal interfaces supports a wave mode, and by proper choice of the fluid densities, layer depths and wave frequencies one may 'tune' the system to a resonant or near-resonant condition. Experiments were carried out over a range of wave frequencies, and the results are compared with numerical solutions of the resonant interaction equations using the analytically derived interaction coefficients for the experimental model.

2. Theoretical results

Consider the evolution of a two-dimensional (x, z) wave in a density stratified fluid confined between two infinite horizontal planes separated by a distance h. The stratification, characterized by the Brunt–Väisälä frequency $N(z)$, is allowed to vary in the vertical and the Boussinesq approximation is invoked. Then, scaling all lengths by h, time with a characteristic Brunt–Väisälä frequency N_0, and velocity components with $N_0 h$, the dimensionless equations of motion can be written as

$$\sigma_t + N^2\psi_x + J(\sigma, \psi) = 0, \tag{2.1}$$

and

$$(\partial^2_{tt}\nabla^2 + N^2\partial^2_{xx})\,\psi + \{J(\sigma, \psi)\}_x + \{J(\nabla^2\psi, \psi)\}_t = 0, \tag{2.2}$$

where $J(a, b)$ is the Jacobian. A stream function ψ has been introduced from which the horizontal and vertical velocities ψ_z and $-\psi_x$ respectively, can be computed, and σ represents the perturbation buoyancy $(g\rho'/\rho_0 h N_0^2)$, where ρ_0 is the mean density and ρ' is the departure from the local undisturbed value $\rho_s(z)$. The first equation states that the density is conserved along the streamlines in the absence of diffusion and the latter equation, derived from the vorticity equation, brings forth the basic linear internal-wave operator.

Denoting the amplitude of the fundamental wave mode with wavenumber k and frequency ω by the small non-dimensional parameter ϵ, a solution of the above equations can be found having the form

$$\begin{aligned}\psi &= \epsilon\phi(z)\,(A(\xi, \tau)\,E + A^*E^{-1}) + \epsilon^2\left\{-i\frac{\partial\phi}{\partial k}\,(A_\xi E - A^*_\xi E^{-1})\right.\\ &\quad\left. + \left(\frac{k}{\omega}\right)^3\theta(z)\,(A^2E^2 + A^{*2}E^{-2}) + \Phi(z)\,|A|^2\right\} + \epsilon^3\psi^{(3)} + \dots, \qquad (2.3)\\ E &= \exp i(kx - \omega t),\end{aligned}$$

and

$$\sigma = \epsilon \frac{k}{\omega} N^2 \phi (AE + A^* E^{-1}) + \epsilon^2 \left\{ -i \frac{N^2}{\omega} \left[\phi \left(1 - \frac{C_g}{C} \right) + k \frac{\partial \phi}{\partial k} \right] (A_\xi E - A_\xi^* E^{-1}) \right.$$
$$\left. + \left(\frac{k}{\omega} \right)^4 [N^2 \theta - \tfrac{1}{2} C^2 \phi^2 (N^2)'] (A^2 E^2 + A^{*2} E^{-2}) + \Sigma(z) |A|^2 \right\} + \ldots, \tag{2.4}$$

providing the amplitude function $A(\xi, \tau)$ (where A^* denotes the complex conjugate) satisfies the equation

$$i(A_\tau + C_g A_\xi) = \epsilon \{ -\lambda A_{\xi\xi} + \nu |A|^2 A \} + O(\epsilon^2). \tag{2.5}$$

The variables $\xi = \epsilon x$ and $\tau = \epsilon t$ are slow space and time scales and the function $\phi(z)$ satisfies the familiar eigenvalue equation

$$\phi'' + k^2 \left(\frac{N^2(z)}{\omega^2} - 1 \right) \phi = 0, \quad \phi(0) = \phi(1) = 0. \tag{2.6}$$

The parameter C_g is the group velocity, which is defined in terms of the eigenfunction ϕ and the phase speed $C = \omega / k$ by

$$C_g = C \left[1 - \omega^2 \frac{\int_0^1 \phi^2 \, dz}{\int_0^1 N^2(z) \phi^2 \, dz} \right] \leqslant C. \tag{2.7}$$

This shows clearly that the group speed of a given wave mode is always less than or equal to (at $k = 0$) the phase speed for that mode. The remaining parameters in the evolution equation (2.5) have the definitions

$$\lambda = \tfrac{1}{2} \omega''(k) = \frac{\omega}{2k^2} \left\{ -3 \frac{C_g}{C} \left(1 - \frac{C_g}{C} \right) + 2k \left(1 - \frac{C_g}{C} \right) \frac{\int_0^1 N^2 \phi \frac{\partial \phi}{\partial k} \, dz}{\int_0^1 N^2 \phi^2 \, dz} - 2k\omega^2 \frac{\int_0^1 \phi \frac{\partial \phi}{\partial k} \, dz}{\int_0^1 N^2 \phi^2 \, dz} \right\} \tag{2.8}$$

and

$$\nu = -\frac{\omega}{2k^2} \frac{\int_0^1 \phi (Q_0 + Q_2) \, dz}{\int_0^1 N^2 \phi^2 \, dz}, \tag{2.9}$$

where

$$Q_0 = k^2 \phi \left\{ \Sigma' - C \left(\Phi''' + 2k^2 \frac{N^2}{\omega^2} \Phi' \right) \right\},$$

$$Q_2 = 2 \frac{k^6}{\omega^4} \left\{ \phi \theta (N^2)' + 3C^2 \left[\left(\frac{\phi^3}{3} \right)' (N^2)' + \frac{\phi^3}{4} (N^2)'' \right] \right\}.$$

The functions $\theta(z)$ and $\Phi(z)$ are defined by the inhomogeneous equations

$$\theta'' + \left[\frac{N^2}{C^2} - (2k)^2 \right] \theta = \phi^2 (N^2)', \tag{2.10}$$

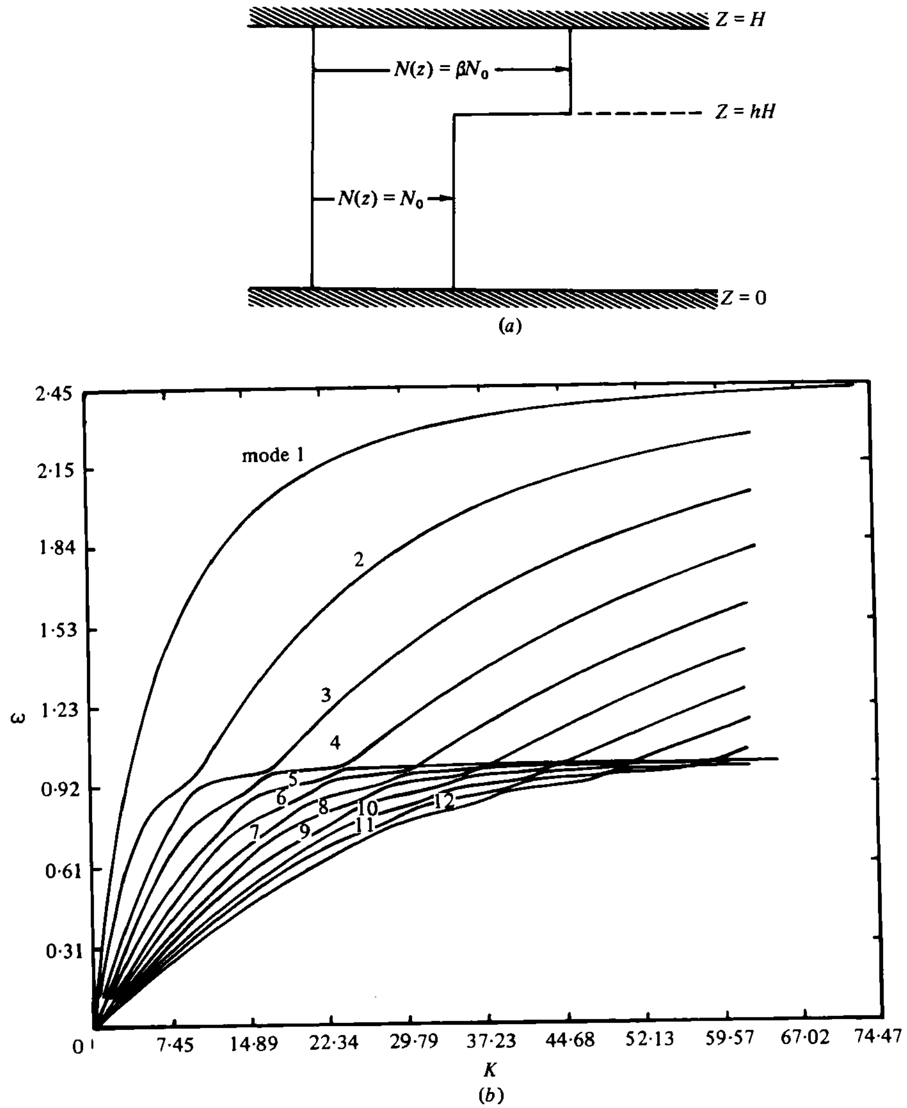

FIGURE 1. (*a*) Schematic diagram of the two layer thermocline. (*b*) Dispersion relation for the two-layer model with parameters $h = 0{\cdot}8$, $\beta = 2{\cdot}5$.

and

$$\Phi'' + \frac{N^2}{C_g^2}\Phi = -\frac{1}{CC_g^2}\left\{\left(1-\frac{C_g}{C}\right)\left(1+2\frac{C_g}{C}\right)N^2(\phi^2)' - 2\left(\frac{C_g}{C}\right)^2\phi^2(N^2)'\right\}. \qquad (2.11)$$

The function $\Sigma(z)$ is related to $\Phi(z)$ by

$$\Sigma(z) = \frac{N^2}{C_g}\Phi + \frac{k^2}{\omega^2}\left\{\phi^2(N^2)' + \left(\frac{C}{C_g}-1\right)N^2(\phi^2)'\right\}. \qquad (2.12)$$

Equation (2.10) and (2.11) require that the resonance conditions $C_m(2k) \simeq C_n(k)$ and $C_m(0) \simeq C_{g_n}(k)$ respectively, are not satisfied. The first condition defines a second-harmonic resonance which is possible for modes m lower than the fundamental

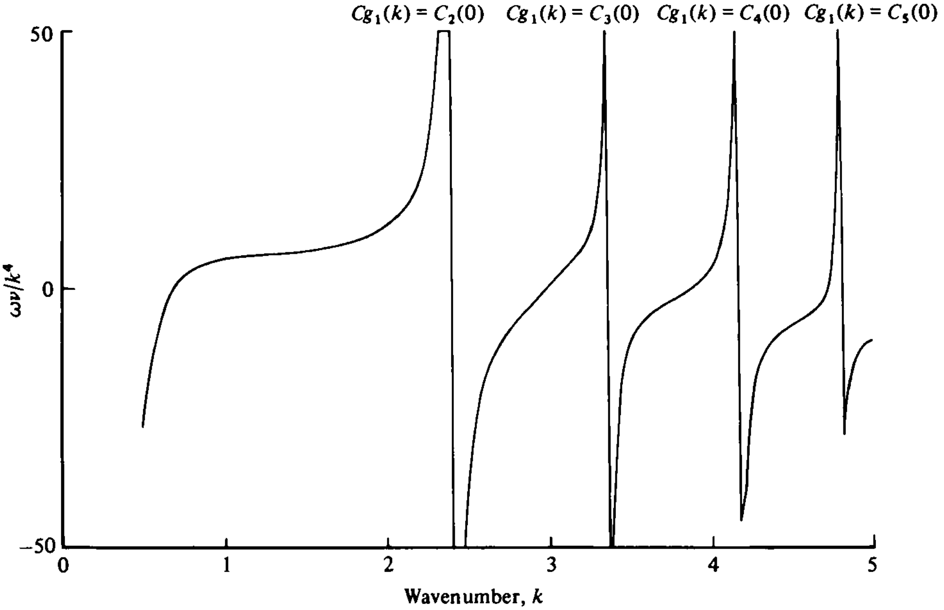

FIGURE 2. Normalized coefficient of self-interaction term in nonlinear Schrödinger equation for two-layer thermocline model. Note the existence of several singularities corresponding to resonances with higher-order modes.

mode n. The second condition defines a resonance which can occur between the fundamental short-wave mode n and higher long-wave modes m. When either of these resonance conditions are satisfied, the single mode evolution described by (2.5) breaks down because the coefficient ν is singular. The multi-modal theory for these resonant cases has been discussed by Djordjevic & Redekopp (1977) and Grimshaw (1977).

Our primary interest here centres on the long-wave–short-wave resonance. However, before briefly outlining the theory for that interaction, we present calculations of the dispersion relation and the evaluation of ν for a thermocline model which emphasizes the ubiquitous nature of this resonance case in oceanic environments. The model and the corresponding dispersion diagram is shown in figure 1. The computation of the coefficient ν for the lowest mode is presented in figure 2 where the singularities arising from a matching of the long-wave phase speeds $C_m(0)$, $m = 2, 3, \ldots$, with the group speed $Cg_1(k)$ is prominent. The resonance bandwidth is quite broad and occupies a significant range of wavenumber space. The results for this model also have important implications regarding a single internal-wave mode governed by (2.5) in the off-resonant bands. It has been established (cf. Hasimoto & Ono 1972) that a periodic wavetrain solution of (2.5) is unstable to modulational disturbances whenever $\lambda\nu < 0$ and that the growth rate of these disturbances is proportional to the absolute value of the coefficient ν. Reference to figure 1 shows that the curvature λ of the dispersion curve has several reversals in sign as k increases. Since ν in general does not change sign at the same values of k, modulationally unstable bands can be expected to abound in any realistic oceanic environment. The product $\lambda\nu$ also changes sign at those wavenumbers where ν has a simple zero and the magnitude of ν can achieve rather large values, even in the non-resonant bands. Hence, the growth rate of the side-band instability can be quite large. Another point worth emphasizing is that the mean flow (or long-wave component) driven by an internal wave packet (cf. equations (2.11) and (2.12)) will be strong in those regions where the *vertical gradient* of the Brunt–Väisälä frequency is large. Such regions abound in most natural thermoclines.

In the vicinity of those resonant bands where $C_{g_n}(k) \simeq C_m(0)$, a consistent asymptotic solution of equations (2.1) and (2.2) has the form

$$\psi = \epsilon\phi(z)\,(S(\xi,\tau)E + S^*E^{-1}) + \epsilon^{\frac{4}{3}}\Phi(z)\,L(\xi,\tau) + \dots \tag{2.13}$$

and

$$\sigma = \epsilon\frac{k}{\omega}N^2\phi(SE + S^*E^{-1}) + \epsilon^{\frac{4}{3}}\frac{N^2}{C_g}\Phi(z)\,L(\xi,\tau) + \dots . \tag{2.14}$$

The short-wave envelope function is here denoted by $S(\xi,\tau)$ and the long-wave amplitude by $L(\xi,\tau)$. The function $\phi(z)$ satisfies the same eigenvalue problem (2.6) as before, but $\Phi(z)$ is a free long-wave mode satisfying the homogeneous form of (2.11). Solvability requirements at the next order in the expansion yield the evolution equations

$$iS_\tau + \lambda S_{\xi\xi} = \nu_1 SL + O(\epsilon^{\frac{2}{3}}), \tag{2.15a}$$

$$L_\tau = \alpha(|S|^2)_\xi + O(\epsilon^{\frac{2}{3}}), \tag{2.15b}$$

where now ξ and τ have definitions

$$\xi = \epsilon^{\frac{2}{3}}(x - C_g t) = X - C_g T, \quad \tau = \epsilon^{\frac{4}{3}}t = \epsilon^{\frac{2}{3}}T. \tag{2.16}$$

The time scale here is $O(\epsilon^{-\frac{4}{3}})$ compared with $O(\epsilon^{-2})$ for the single-mode case described by (2.5). This evolution system shows that the long wave, which is of order $\epsilon^{\frac{1}{3}}$ compared to the short wave, is generated by spatial gradients in the envelope of the short wave and the short wave is detuned and modulated by the interaction of itself with the long wave. These equations represent the appropriate limit of the resonant three-wave interaction equations when one member of the triad is very long and the other two members are only slightly separated in wavenumber space. The coefficients ν_1 and α in (2.15) are given by the following quadratures:

$$\nu_1 = -\frac{k(C/C_g)^2}{2\int_0^1 N^2\phi^2\,dz}\int_0^1\left[\left(1-\frac{C_g}{C}\right)\left(1+2\frac{C_g}{C}\right)N^2\phi^2\Phi' + \left(1+\frac{C_g}{C}\right)\phi^2\Phi(N^2)'\right]dz \tag{2.17}$$

and

$$\alpha = -\frac{C_g/C}{2\int_0^1 N^2\Phi^2\,dz}\int_0^1\left[\left(1-\frac{C_g}{C}\right)\left(1+2\frac{C_g}{C}\right)N^2\Phi(\phi^2)' - 2\frac{C_g}{C}\Phi\phi^2(N^2)'\right]dz. \tag{2.18}$$

The coefficient λ has the same definition as before.

For our later discussion of experimental results, it is important to consider the linear stability of a uniform wavetrain solution of the coupled system (2.15). Hence, we write

$$S = S_0\{1 + s(\xi,\tau)\}\exp\{-i\nu_1 L_0\tau\}, \quad L = L_0\{1 + l(\xi,\tau)\}, \tag{2.19}$$

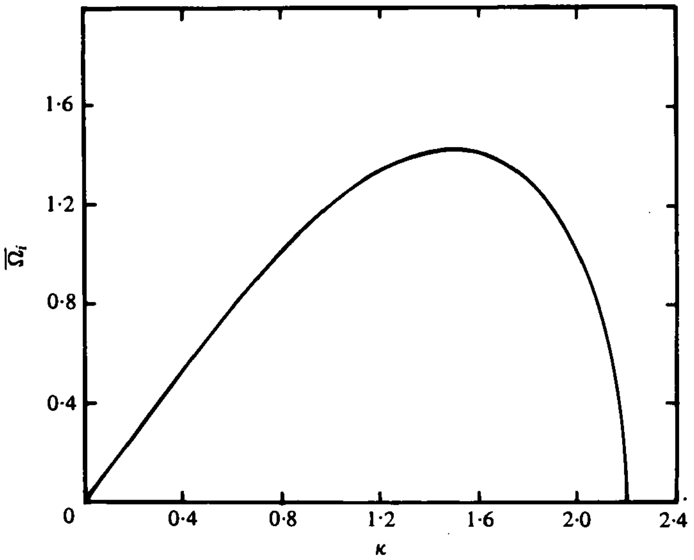

Figure 3. Linear stability diagram for long-wave–short-wave resonance equations.

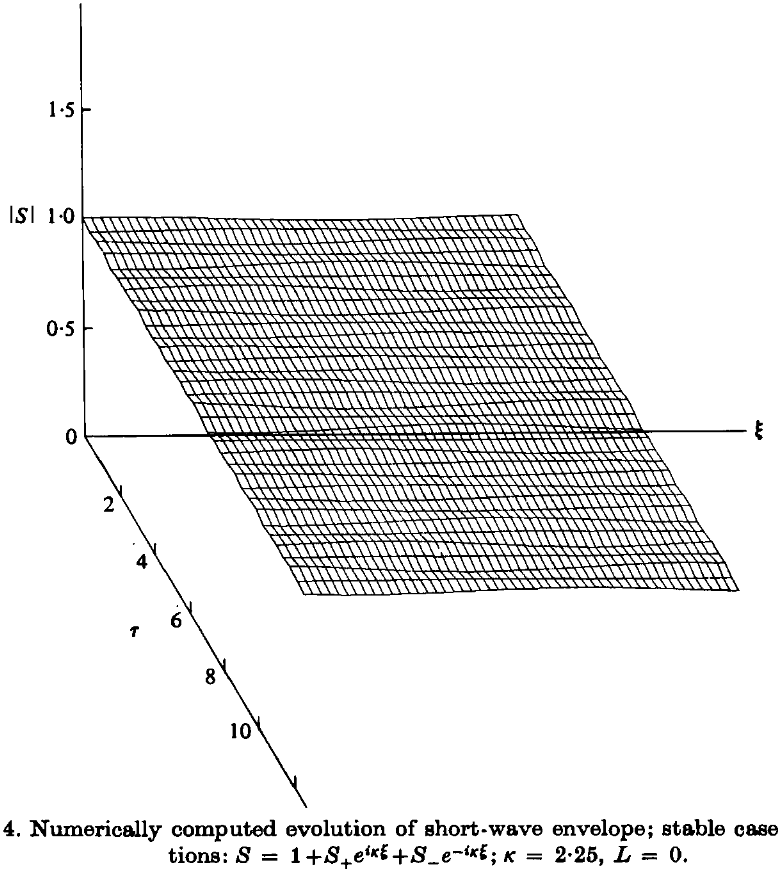

Figure 4. Numerically computed evolution of short-wave envelope; stable case. Initial conditions: $S = 1+S_+e^{i\kappa\xi}+S_-e^{-i\kappa\xi}$; $\kappa = 2{\cdot}25$, $L = 0$.

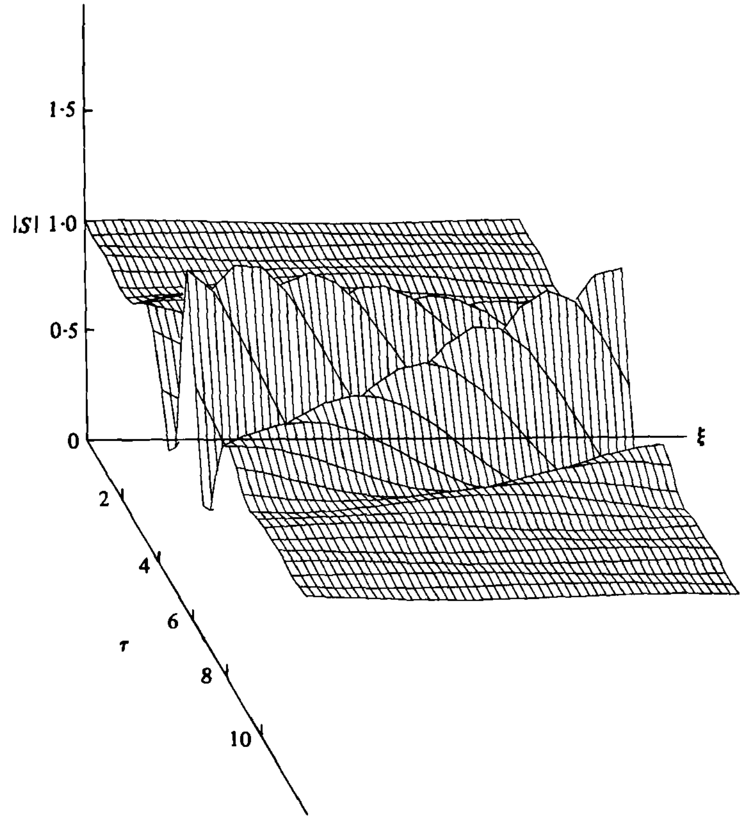

FIGURE 5. Numerically computed evolution of short-wave envelope; unstable case. Initial conditions: $S = 1+S_+e^{i\kappa\xi}+S_-e^{-i\kappa\xi}$; $\kappa = 2\cdot10$, $L = 0$.

where $s(\xi,\tau)$ and $l(\xi,\tau)$ represent small perturbations to the uniform wavetrain and S_0 and L_0 are order-one constants. After writing

$$S = S_+\exp\{i(K\xi-\Omega\tau)\}+S_-\exp\{-i(K\xi-\Omega^*\tau)\} \tag{2.20}$$

and substituting into the evolution system and linearizing, one obtains the eigenvalue relation

$$\Omega^3-(K^2\lambda)^2\Omega-2\nu_1\alpha\lambda K^3|S_0|^2 = 0. \tag{2.21}$$

The uniform solution is found to be unstable whenever the condition

$$3^{\frac{3}{2}}|\nu_1\alpha|\,|S_0|^2 > \lambda^2K^3 \tag{2.22}$$

is satisfied. Observe that one can always find a modulation wavelength long enough to satisfy the instability criterion. Furthermore, when the dispersion λ tends towards zero, a common occurrence in environments with variability in $N(z)$ as evidenced in figure 1, any modulation wavelength destabilizes an internal wave and, in fact, does so even for very small primary-wave amplitudes. Observe also that the instability criterion is independent of the long-wave amplitude. Hence, a resonant long wave is unstable with respect to, and can be generated by, sufficiently long modulations of the short wave. It is important to point out that the instability is unidirectional in the sense that the long wave cannot generate the short wave if the short wave is

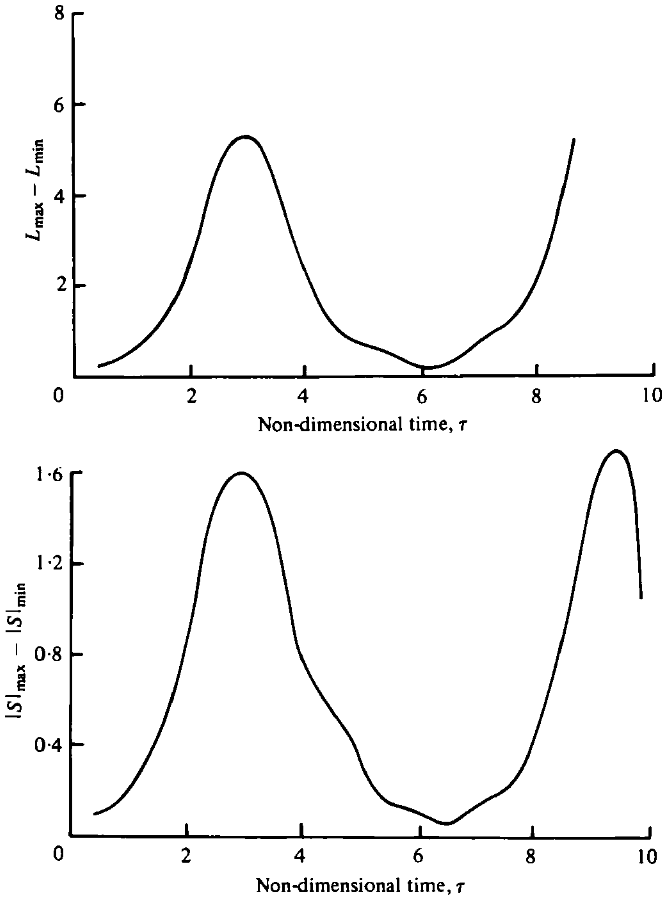

FIGURE 6. Numerical solution to resonance equations demonstrating near recurrence. Initial conditions: $S = 1 + S_+ e^{i\kappa\xi} + S_- e^{-i\kappa\xi}$; $\kappa = 1{\cdot}51$, $L = 0$.

initially zero. The growth rate for the unstable mode of (2.22) is presented in a universal form in figure 3. The wavenumber K and frequency Ω have been normalized so that the eigenvalue relation assumes the form

$$\bar{\Omega}^3 - \kappa^4\bar{\Omega} + 4\kappa^3 = 0,$$

$$\Omega = |\lambda| \left|\frac{\nu_1\alpha}{2\lambda^2} S_0^2\right|^{\frac{2}{3}} \bar{\Omega}, \quad K = \operatorname{sgn}(\nu_1\alpha\lambda) \left|\frac{\nu_1\alpha}{2\lambda^2} S_0^2\right|^{\frac{1}{3}} \kappa. \tag{2.23}$$

The maximum normalized growth rate is 1·42 occurring at a wavenumber of 1·51. The unstable range is $0 < \kappa < 2^{\frac{1}{3}} \times 3^{\frac{1}{2}} = 2{\cdot}182$ in terms of the normalized variables.

The long-time behaviour of the modulational instability described above has been investigated by numerically solving the normalized version of (2.15)

$$iS_\tau + S_{\xi\xi} = SL, \quad L_\tau = -2(|S|^2). \tag{2.24}$$

The normalization used here is consistent with the growth-rate characteristics shown in figure 3 and the eigenvalue relation (2.23). The numerical scheme used to integrate these equations is the time-stepping leap-frog method described by Fornberg (1977).

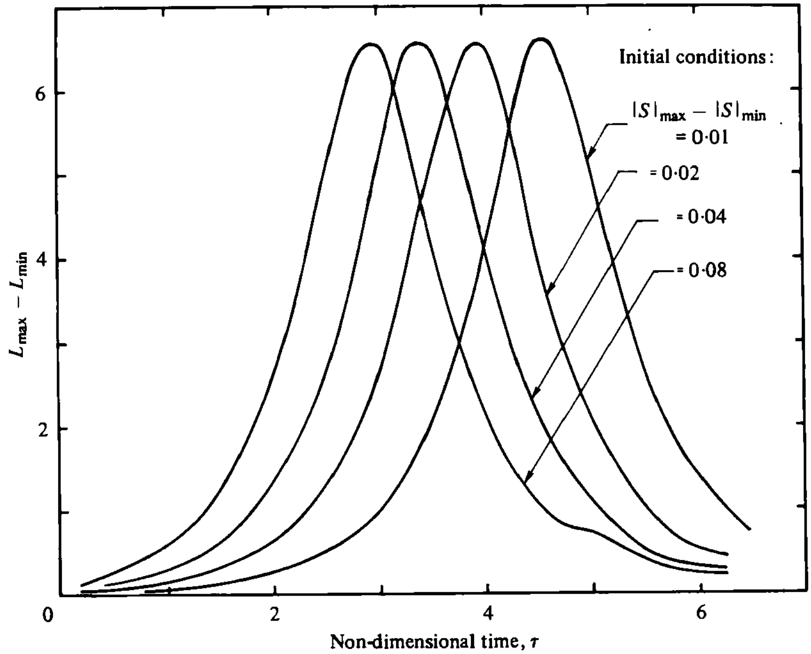

FIGURE 7. Effect of initial modulation amplitude upon long-wave evolution. Initial conditions: $S = 1+S_+e^{i\kappa\xi}+S_-e^{-i\kappa\xi}$: $\kappa = 1{\cdot}51$, $L = 0$.

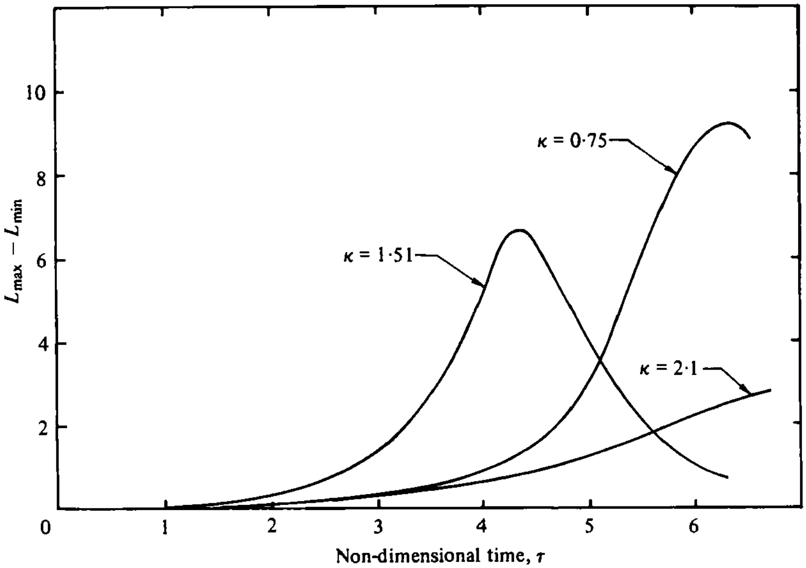

FIGURE 8. Effect of initial modulation wavelength upon long-wave evolution. Initial conditions: $S = 1+S_+e^{i\kappa\xi}+S_-e^{-i\kappa\xi}$; $|S|_{max}-|S|_{min} = 0{\cdot}01$, $L = 0$.

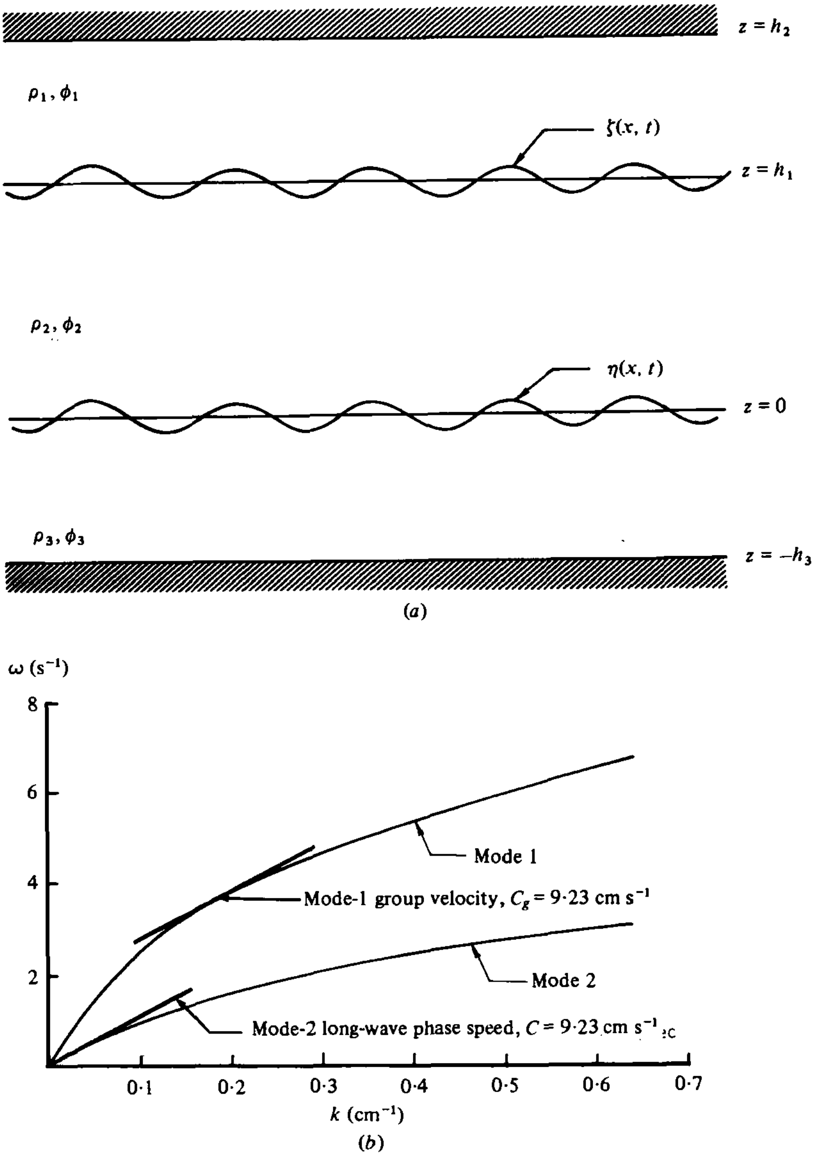

FIGURE 9. (*a*) Three-layer model. (*b*) Linear eigenvalue solution for three-layer system.

Figures 4 and 5 show calculations for initial modulation wavenumbers of (2.25) and (2.10). The first case is stable on a linear basis and the second case is unstable. The long-time evolution confirms that $\kappa = 2{\cdot}182$ is the stability boundary. The calculations also show that the initial growth rate agrees well with linear theory, but decreases as the modulation grows. We have also investigated the effect of the initial modulation amplitude ΔS_0 and wavelength $2\pi/\kappa$ on the long-time evolution. The initial conditions are characterized by the expressions

$$\Delta S_0 = |S|_{\max} - |S|_{\min},$$
$$S(\xi, \tau = 0) = 1 + S_+ e^{i\kappa\xi} + S_- e^{-i\kappa\xi}. \qquad (2.25)$$

The initial long-wave amplitude is taken to be zero since it results only in a constant frequency shift of the short wave and can be removed by a simple scaling. Figure 6 shows the results of a calculation where near-perfect recurrence was observed. The recurrence time was about 6 non-dimensional time units for the case where the initial condition corresponds to the most unstable one on a linear basis. Figure 7 shows the effect of the initial modulational amplitude on the evolution of the long wave holding the disturbance wavelength fixed. The results are interesting in that the total energy deposited into the long-wave mode by the resonance mechanism is very insensitive to the initial perturbation amplitude. However, the recurrence time does depend on ΔS_0. In figure 8, the effect of the perturbation wavelength on the evolution of the long-wave mode is exhibited. The initial growth rate is greatest for $\kappa = 1{\cdot}51$, which is consistent with linear theory. However, the energy transport to the long wave is greater for the longer perturbation $\kappa = 0{\cdot}75$, although the time required to achieve saturation is shortest for the linearly most unstable disturbance. The strongest interaction on the long-time scale is therefore seen to depend intimately on the nonlinear coupling and is not well described by the linear theory.

Probably the simplest environment in which to explore this interaction experimentally for internal waves is a three-layer system of homogeneous fluids having different densities, as shown schematically in figure 9(*a*). By a proper choice of the various densities and layer thicknesses, one may 'tune' the system to a resonant condition whereby the group velocity of the shorter mode and the phase velocity of the longer mode are nearly equal. Thus, all of the physics relevant to the long-wave/short-wave resonant interaction are contained in this simple configuration while many extraneous processes like multi-modal interactions, etc., which could occur in a continuously stratified system are eliminated. The three-layer dispersion diagram for the experimental test conditions is shown in figure 9(*b*), where the long-wave/short-wave resonance condition is identified. The derivation of the interaction coefficients in (2.15) for this system, as well as the generalization of the long-wave equation to off-resonant conditions, is presented in the appendix. As shown there (cf. equation (A 8)), the generalized long-wave equation for this flow model is

$$\mathscr{L}_w L_T = \epsilon^{\frac{2}{3}}\alpha(|S|^2)_{XXXXX}. \tag{2.26}$$

Here, $\mathscr{L}_w$ is a fourth-order wave operator

$$\mathscr{L}_w \equiv (\partial^2_{TT} - C^2_{12}\partial^2_{XX})(\partial^2_{TT} - C^2_{23}\partial^2_{XX}) - \left(1 - \frac{C^2_{12}}{C^2_0}\right)\left(1 - \frac{C^2_{23}}{C^2_0}\right)\partial^4_{TTTT}, \tag{2.27}$$

corresponding to long waves propagating in both directions on both interfaces. The speed C_0 is the long-wave phase speed for a given mode and C_{12} (C_{23}) are the respective long-wave phase speeds when the lower-layer (upper-layer) thickness vanishes so that the system reduces to a two-layer one. Rewriting this operator in terms of the convecting co-ordinates (2.16) and assuming that C_0 is close to C_g and C_{23}, say, but removed from C_{12}, we may approximate the operator by

$$\mathscr{L}_w \cong -(C^2_g - C^2_{12})(C_g + C_{23})\frac{\partial^3}{\partial\xi^3}\{\epsilon^{\frac{2}{3}}\partial_\tau - (C_g - C_{23})\partial_\xi\}. \tag{2.28}$$

Note that this approximation becomes less exact as the system moves away from resonance. One useful aspect of the experimental study is to define the bandwidth

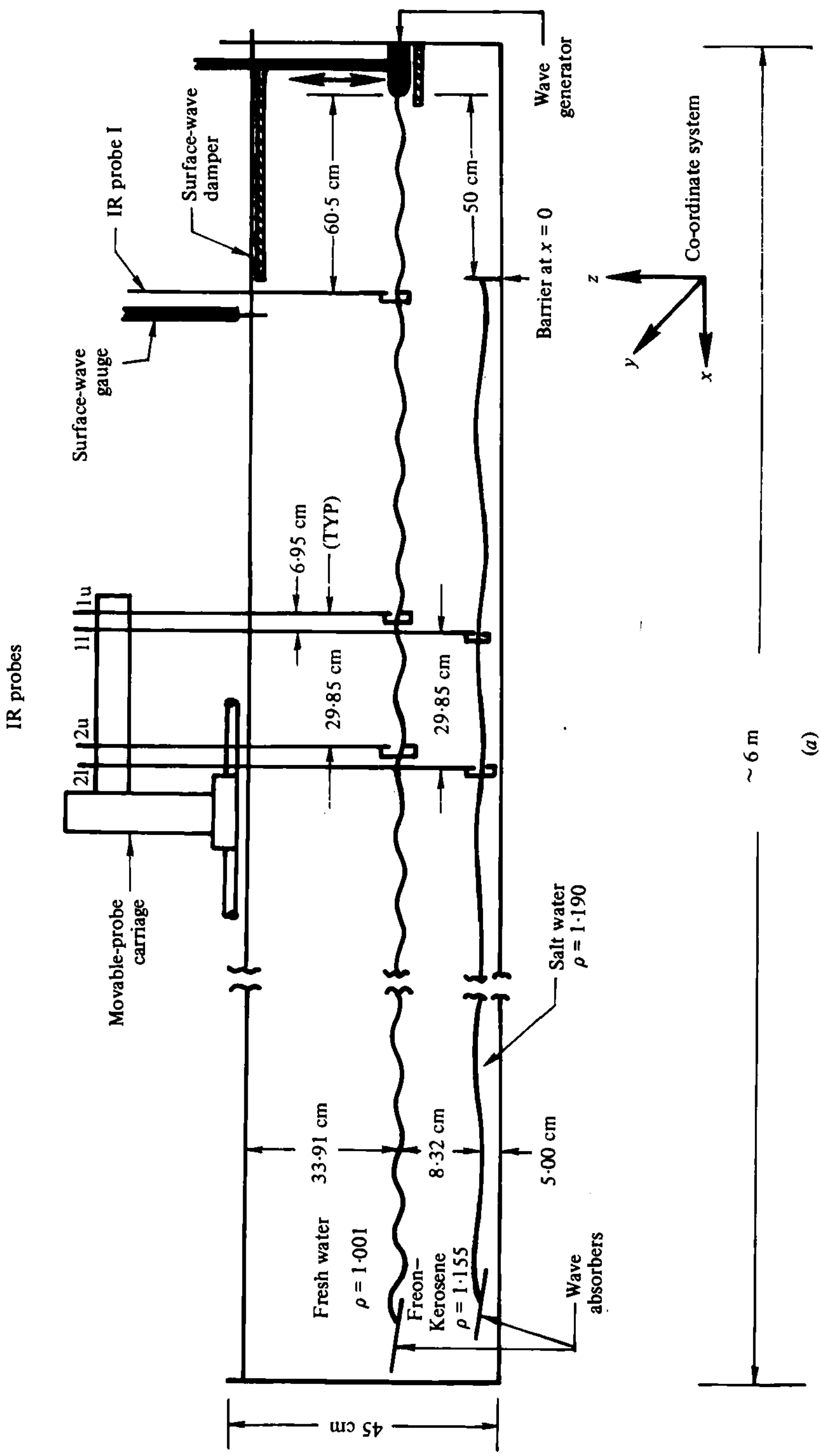

(*a*)

FIGURE 10(*a*). For legend see p. 380.

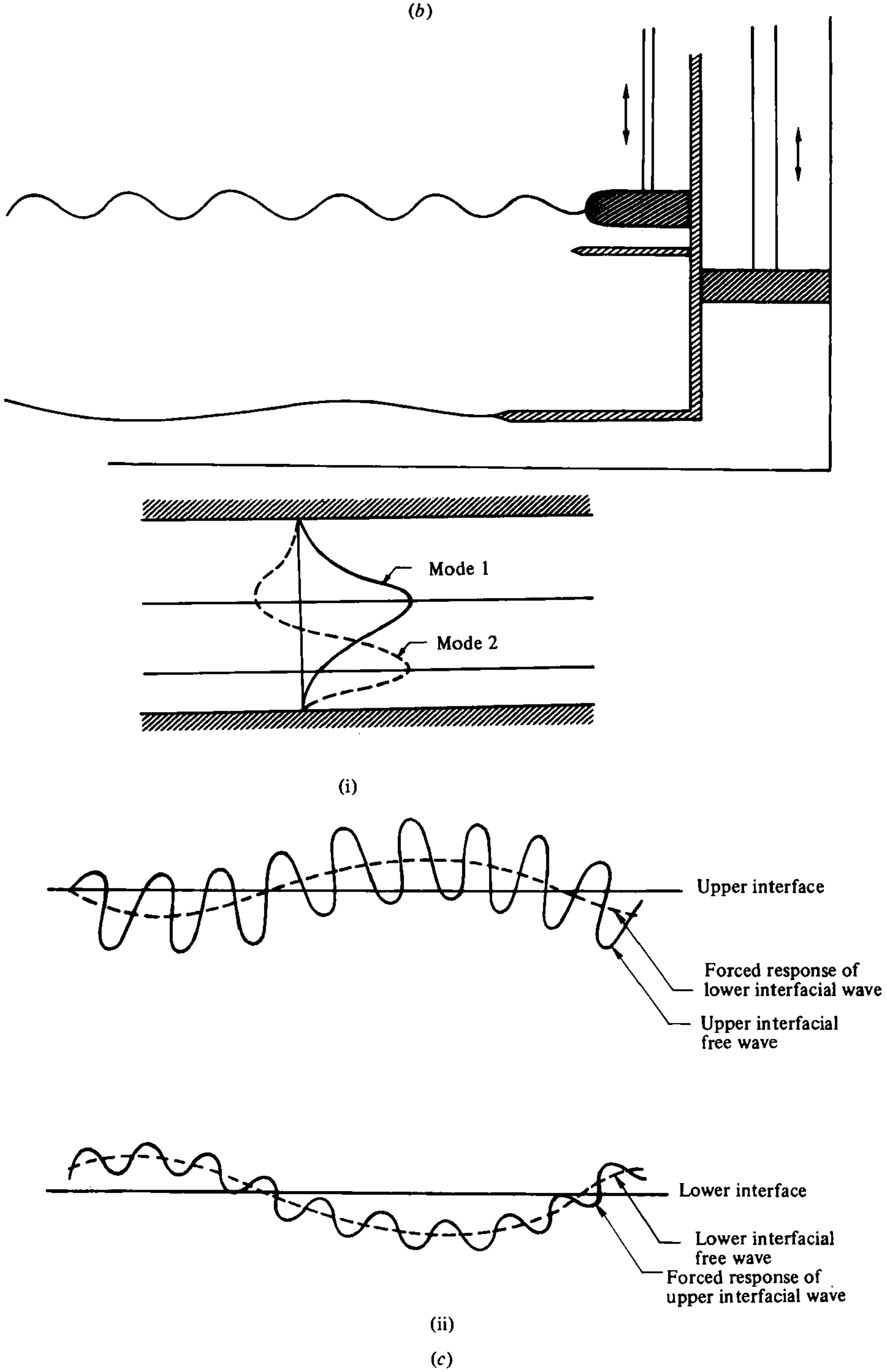

FIGURE 10. Schematic representation of (*a*) the internal-wave facility and (*b*) the two-wavemaker configuration. (*c*) Three-layer eigenfunctions: (i) schematic representation of mode-1 and mode-2 eigenfunctions; (ii) schematic representation of interfacial displacements when both modes are present.

for which this near-resonance theory (i.e. equation (2.28)) is valid. From equation (2.28), the bandwidth of the resonance is $O(\epsilon^{\frac{2}{3}})$. Thus, within this region the general long-wave equation, given by equation (2.27), may be approximated by the expression

$$L_\tau + C_0 \Delta L_\xi = \frac{\alpha}{C_g(C_g + C_{23})(C_g^2 - C_{12}^2)} (|S|^2)_\xi, \tag{2.29}$$

$$\Delta = \frac{C_0 - C_g}{\epsilon^{\frac{2}{3}} C_0}.$$

This is the form of the equation referred to subsequently for use in correlating the theoretical and experimental results.

3. Experimental results

The preceding analysis has identified an interesting modal interaction which describes how energy initially deposited into waves of relatively short horizontal extent may be transferred to higher-order internal wave modes of significantly longer wavelength. In the present section, we present the results of an experimental investigation of this interaction in an idealized situation, so that detailed comparisons with the theory may be made.

3.1. *Experimental apparatus and procedure*

The experiments to be described were performed in the internal wave facility shown schematically in figure 10(*a*). The wave tank, constructed from reinforced ½-inch Plexiglas, has an overall length of 6 m with a 45 × 60 cm cross-section. The fluid medium chosen to study the long-wave/short-wave resonance phenomenon consists of three mutually immiscible homogeneous layers created using (in order of increasing density) fresh water ($\rho_1 = 1{\cdot}001$, $h_1 = 33{\cdot}91$ cm), a mixture of Freon and kerosene ($\rho_2 = 1{\cdot}155$, $h_2 = 8{\cdot}32$ cm), and saturated salt water ($\rho_3 = 1{\cdot}19$, $h_3 = 5{\cdot}00$ cm). For the specific densities and layer thicknesses chosen, the two internal modes for this system correspond to a high-frequency short wave, propagating on the upper interface, and a low-frequency long wave which propagates on the lower interface. The eigenfunctions corresponding to each of these modes is shown schematically in figure 10(*c*), where it is seen that the high-frequency wave has no zero crossings (i.e. a mode 1 wave), and the low-frequency disturbance has one zero crossing (i.e. a mode 2 wave). Figure 10(*c*) also shows the qualitative appearance of the two interfaces when both modes are present. Note that a direct measurement of the energy contained in the mode 1 disturbance may be made by high-pass filtering the upper interfacial signal to remove the forced long-wave response. Similarly, one may measure the energy content of the mode 2 wave by low-pass filtering the lower interfacial signal to remove the forced short-wave response.

As previously mentioned, the primary interest in this experimental study is the generation of a low-frequency long wave by a modulated high-frequency wavetrain. In the present context, this implies that one is interested in generating modulated wavetrains on the upper interface by some mechanical means, and studying the hydrodynamic response of the lower interface to this forcing. The wavemaker utilized to generate such a modulated wavetrain is a modification of the displacement-type

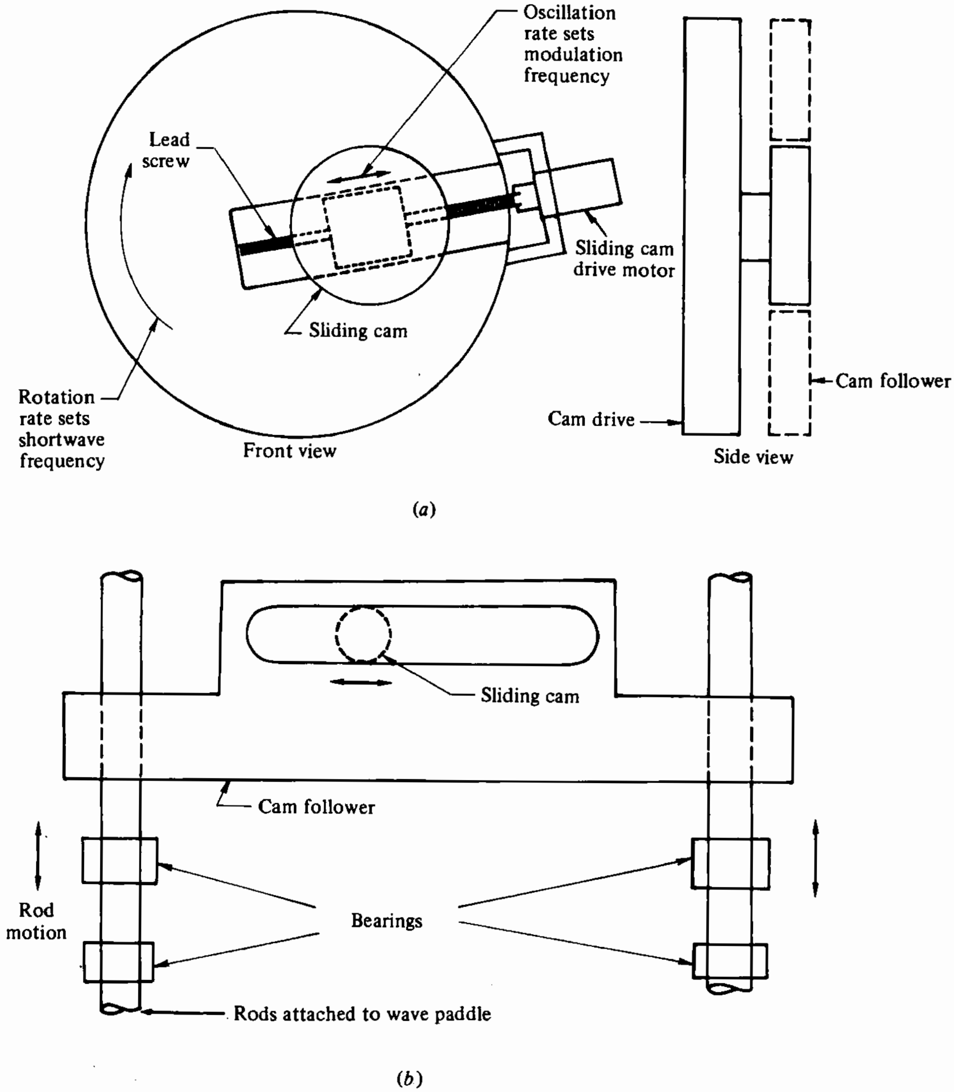

FIGURE 11. Schematic diagram of 'Scotch yoke' used to generate modulated wavemaker displacement. (*a*) Rotating cam drive. (*b*) Cam follower.

device used by Koop & Butler (1981). Essentially, the wave generator consists of a $5 \times 15 \times 45$ cm wave paddle which straddles the upper interface and oscillates sinusoidally in the vertical direction. The wave paddle is coupled to a drive motor through a Scotch yoke (see figure 11). Since the amplitude of the interfacial waves generated by this motion is proportional to the stroke of the displacement, one may modulate this wavetrain by varying the eccentricity of the cam motion in some periodic fashion. This is accomplished by using a second drive motor mounted on the rotating cam (and receiving power through two slip rings) to sinusoidally vary the radial distance of the cam from the axis of rotation.

The typical operating conditions for this wavemaker were such that the modulation period was fixed at 12·83 s, and carrier waves having periods T_{SW}, ranging between 1·1 and 1·925 s were generated. Tests conducted to evaluate the constancy of the wave-generator frequency revealed that roughly 99 % of all the energy lies in a bandwidth of less than ± 0·3 % of the centre frequency. Furthermore, it is noted that the upper interfacial wavetrain exhibited none of the self-modulation characteristics observed by Yates (1978) in a similar modal interaction experiment.

Returning to an examination of figure 10 (*a*), it is observed that a barrier is present on the bottom of the tank which prevents the Freon–kerosene/salt-water interface from extending all the way to the wavemaker. This was done to ensure that the lower interface could not be forced directly by the pressure field associated with the upper interfacial wave generator. The presence of this barrier also provides a well-defined spatial origin for the interaction being studied. Although the bulk of the experimentation to be discussed in this report was performed in this configuration, it is noted that a limited number of preliminary experiments were performed with the barrier removed. In those runs, a second wavemaker was utilized to generate low-frequency waves on the lower interface. This was done in order to study qualitatively the interaction between a pre-existing long wave and an initially unmodulated short wave. Figure 10 (*b*) shows schematically this two-wavemaker configuration.

Figure 10 (*a*) also shows the wave absorption devices which were positioned at the downstream end of the tank. Note that each interface has its own wave absorber. The absorber located on the upper interface proved to be very effective at dissipating the short-wave energy. Using isolated packets of short waves and measuring the amount of energy reflected off the wave absorber, it was ascertained that more than 99·8 % of the short-wave energy is dissipated by the wave absorber. In contrast, however, one finds that the low-frequency wave motion associated with the lower interface is not nearly so easily removed. Tests revealed that only about 75 % of the incident long-wave energy is dissipated in the wave absorber. The remainder reflects back into the test section, propagates upstream (slowly dissipating by viscosity), reflects off the barrier, and once again propagates downstream. Although this problem of long-wave reflection is of some concern it is almost unavoidable in the present system, since a wave absorber designed to dissipate such long waves would occupy an unduly large portion of the test section. For the present, we simply note that the problem exists, and the approach taken to alleviate this difficulty will be discussed in a subsequent section.

The primary diagnostic tool used in this experiment was a newly developed infrared optical interfacial-wave amplitude gauge. A complete discussion of this sensor is given in Koop, Rungaldier & Sherman (1979). The motivation for developing this new gauge came during the preliminary stage of the study when it became clear that the conventional capacitance-type gauges of the type described by Lake *et al.* (1977) were unsuited for the type of internal-wave measurements desired. The principal difficulty seemed to stem from the erratic dynamical behaviour of the fluid meniscus in contact with the probe (this was especially true when the density difference across the interface was very small). Some of the troublesome aspects encountered were d.c. drift, nonlinearity, hysteresis and sensitivity changes.

In the present optical sensor, an infrared emitter is positioned above the interface, and a detector below, as shown schematically in figure 12. Since water is a very good absorber of infrared energy, the radiative intensity measured by the detector is a

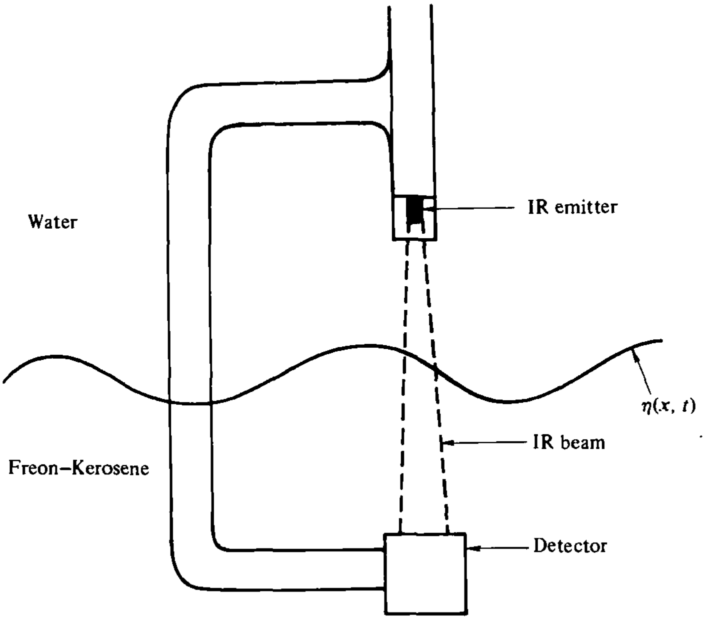

FIGURE 12. Schematic diagram of infrared interfacial wave gauge.

function of the vertical location of the interface which varies according to the wave motion propagating on the interface.

The probe arrangement for this investigation is shown in figure 10(*a*). Probe I is an IR probe positioned 60·5 cm downstream of the wavemaker to monitor the initial wavefield on the upper interface. Also located at this position is a surface wave capacitance gauge which was included to monitor the effectiveness of the surface wave damper. In addition to these sensors, four IR probes (two on each interface) were mounted on a movable platform. The probes, identified as 1u and 2u, monitor the upper interfacial displacements, and are longitudinally displaced by 29·85 cm. The second pair of probes, identified as 1l and 2l, monitor the lower interface and are longitudinally displaced by the same amount. Probes 1u and 1l are separated by 6·96 cm. Finally, a linear variable displacement transducer (LVDT) is used to monitor the displacement of the wave generator.

For the particular choice of ρ_1, ρ_2, ρ_3, h_1, h_2, and h_3 shown in figure 10(*a*) and for a long-wave period $T_{\mathrm{LW}} = 12{\cdot}83$ s, the condition for resonance between the long wave and the short wave occurs when the short-wave period is $T_{\mathrm{SW}} = 1{\cdot}63$ s. In order to study both the resonant interaction, and also some off-resonant conditions, nine test cases were chosen having short-wave periods ranging between $1{\cdot}1 \leqslant T_{\mathrm{SW}} \leqslant 1{\cdot}925$ s. The long-wave period (or modulation period) was kept fixed. For all of these experiments, the initial amplitude of the wavetrain (*not* the wavemaker displacement) was fixed at roughly 1 cm (peak–peak), and the modulation amplitude was fixed at roughly 0·1 cm. One should remember, however, that, because the short-wave group velocity is a function of T_{SW}, the *wavelength* of the modulation varies from case to case even though T_{LW} is held fixed. All of the test conditions are tabulated in table 1.

The test procedure followed in this investigation has two parts. The long-wave/short-wave resonance phenomenon under study arises through an interaction between

Case	T_{SW} (s)	C_{GSW}	λ_{mod} (cm)
1	1·1	6·2	79·5
2	1·2	6·65	85·3
3	1·3	7·20	92·4
4	1·4	7·75	99·4
5	1·5	8·45	108·4
6	1·63	9·10	116·8
7	1·7	9·55	122·5
8	1·8	10·20	130·9
9	1·925	11·20	143·7

TABLE 1. Tabulation of experimental test conditions. $T_{LW} = 12{\cdot}83$ s, $C_{LW} = 9{\cdot}23$ cm s^{-1} for all cases.

a forced modulated wavetrain (mechanically generated by the wavemaker) and the hydrodynamically generated lower interfacial wave. Before proceeding to investigate this coupled system, it is first useful to examine the nature of the energy source for the interaction (*viz.* the upper interfacial wavetrain) in the absence of any coupling with the lower layer. For each value of T_{SW}, then, the first part of the test procedure was to survey the spatial evolution of the *unmodulated* wavetrain as it propagated through the test section. This was done primarily to measure the viscous decay rate for each case, as well as to examine the lateral structure of the carrier waves. Because the wavetrain was unmodulated, one did not have to be concerned about interactions with the lower interface, and the carrier waves propagated as free waves. The measurements were performed at 27 stations, separated longitudinally by 10·16 cm between $0 < x < 280$ cm. At each station about 4 min of data were taken, after which the probe carriage was translated to the next station. Note that, since probes 1u and 2u are displaced by roughly 30 cm, three translations result in probe 1u occupying almost the same longitudinal position that probe 2u occupied at an earlier time. This feature allows for a very useful check on the repeatability and stationarity of the measurements, since at a given longitudinal position one has two measurements made by different probes at different times.

The second part of the test procedure was to study the long-wave/short-wave interaction. For each case, the wave generator produced a modulated wavetrain, and data were taken on both interfaces for 12 minute intervals (corresponding to roughly 50 modulation periods) at 16 longitudinal stations separated by 15·25 cm between $0 < x < 280$ cm. Note that, as in the dissipation measurements, a check on the repeatability of the data exists, since two translations result in probe 1u (or 1l) occupying the same position that probe 2u (or 2l) occupied at an earlier time. Typically, two days of experimentation were required to complete each of the nine test cases.

The outputs of all seven sensors (four carriage-mounted IR probes, IR probe I, the surface wave capacitance gauge, and the wave generator LVDT output) were monitored on an 8 channel oscillograph and recorded on a 14 track FM tape recorder. All of the subsequent data reduction was completed by replaying the taped data and using analog devices for processing.

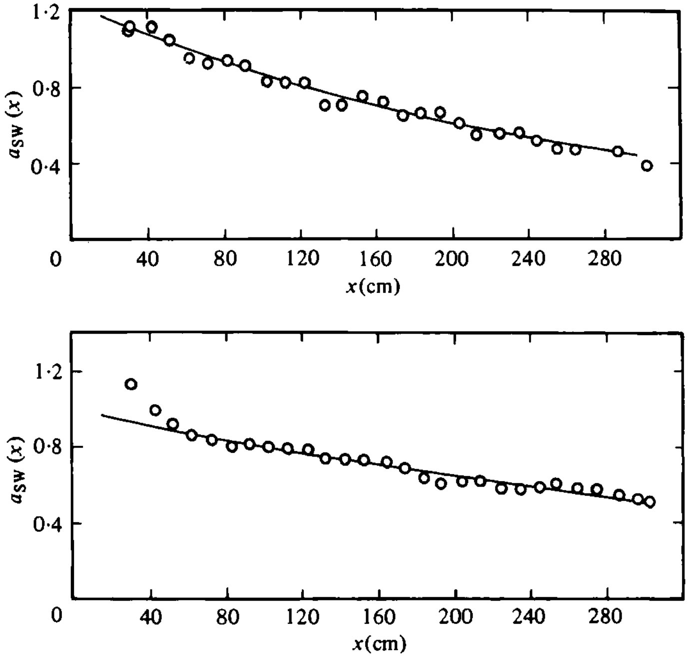

FIGURE 13. Spanwise average of short-wave peak–peak amplitude $a_{sw}(x)$ *vs.* x. (*a*) $T_{sw} = 1{\cdot}3$ s; (*b*) $T_{sw} = 1{\cdot}5$ s. ○, measurements; ——, best least-squares fit of the form

$$a_{sw}(x) = a_{sw}(x = 0) \exp(-D_s x/C_g).$$

3.2. *Viscous dissipation*

For each of the nine test conditions identified in table 1, a series of measurements were made to determine the extent of the viscous dissipation of the upper interfacial wavetrain. Figure 13 presents results for the cases $T_{SW} = 1{\cdot}3$ and $1{\cdot}5$ s. To minimize the effects of any lateral structure, these measurements represent spanwise averages obtained by slowly traversing (3–4 min/traverse) the wave gauges across the tank.† Using these and similar data, a short-wave dissipation constant, D_s, may be defined as

$$a_{SW}(x) = a_{SW}(x = 30 \text{ cm}) e^{-D_s x/C_g},$$

where $a_{SW}(x)$ is the spanwise averaged peak–peak amplitude of the short-wave mode, and $x = 30$ cm represents the first measuring station.

Within the range of operating conditions, D_s varied between $0{\cdot}015 < D_s < 0{\cdot}035\,\text{s}^{-1}$. In terms of wave attenuation, this corresponds to amplitude decreases through the test section of between 30–80 %. It is significant to note here that, particularly for the higher-frequency waves, viscous dissipation has a non-negligible effect upon the short-wave amplitude. In the resonant interaction model, however, such effects are not included. Clearly, some modification to the invisid theory will be required if detailed

---

† Although we will not pursue the topic here, these data also revealed the existence of an interesting modulation structure in the *spanwise* direction (even though the wave generator was programmed to make uniform wavetrains). Subsequent tests revealed that such spanwise structure had little or no effect upon the long-wave/short-wave resonant interaction under investigation, so that further discussion of this phenomenon is not deemed warranted here. However, in a separate paper (Koop 1981) the character of this spanwise modulation is discussed in more detail.

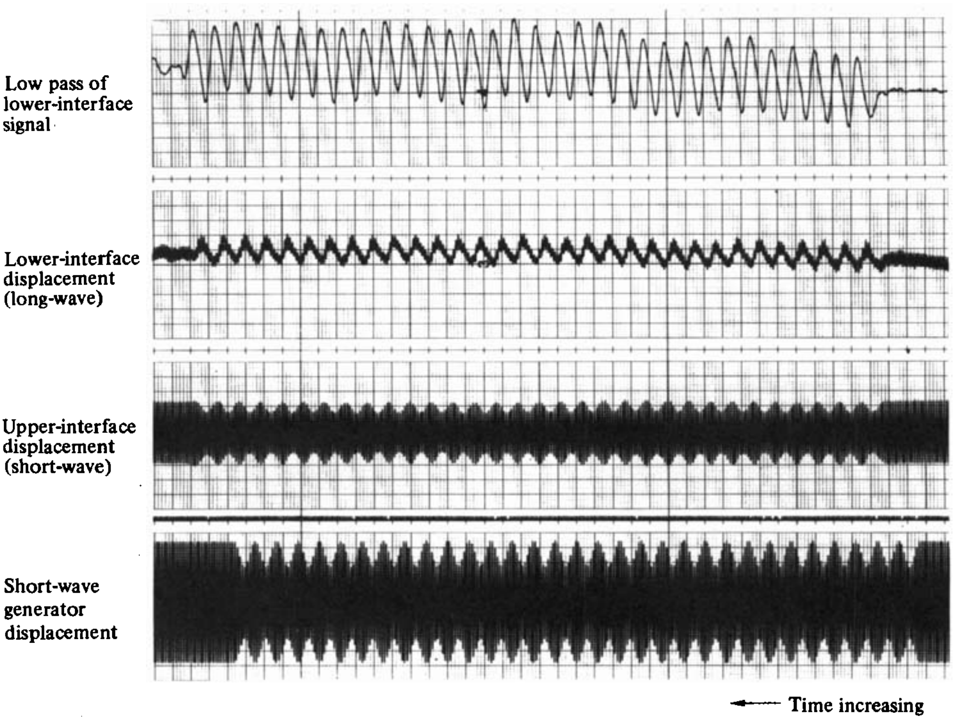

FIGURE 14. Example of modal interchange of energy.

quantitative comparisons with the data are to be made. This problem will be returned to subsequently.

3.3. *Long-wave/short-wave interaction; qualitative results*

The theoretical analysis described in §2 provides a framework for interpreting the experimental results of the resonant interaction of two internal wave modes of disparate length and time scales. The basic conclusions one draws from this theory are that at resonance the long wave is forced by spatial gradients in the short-wave envelope, and the dispersion of the short-wave mode is balanced by a nonlinear interaction with the long wave. Furthermore, the theory predicts that the interaction may proceed in either of two ways:

(*a*) A modulated short wave acts as an energy source for the growth of the long wave. In this case, the larger the spatial gradients of the short-wave envelope, the stronger the interaction.

(*b*) A pre-existing long wave acts to modulate an initially uniform short-wave wavetrain.

Clearly, at certain phases of the interaction, both of these effects will be important. Before proceeding to a detailed discussion of the experimental measurements, it is worth while to present some qualitative results which demonstrate some of the important features of the resonant interaction. Typically, the experiments were performed by generating a modulated wavetrain on the upper interface and observing the hydrodynamic response of the lower interface to this wave-induced forcing.

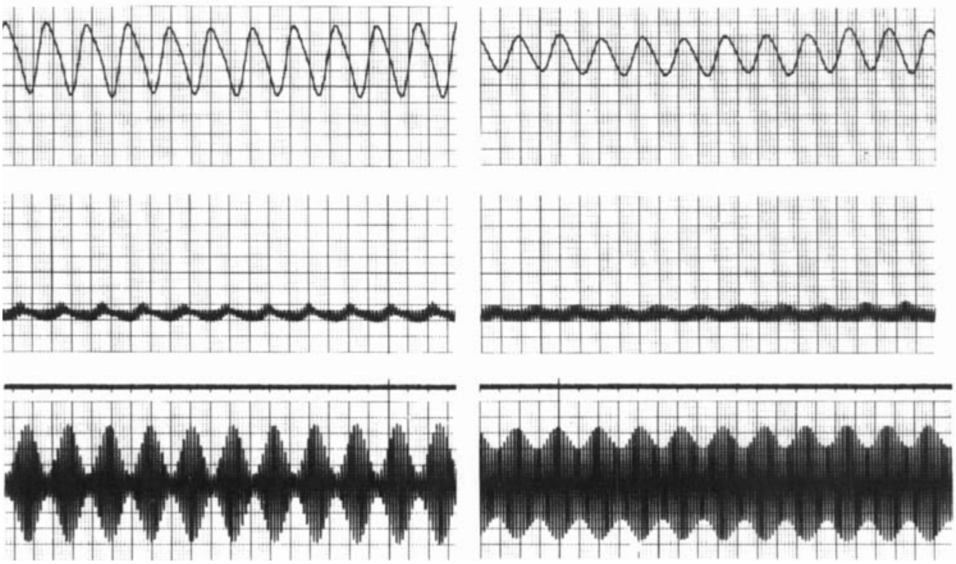

FIGURE 15. Effect of modulation amplitude upon mode-2 wave.

Figure 14 shows an oscillograph record of such an experiment performed near the resonant period $T_{SW} = 1{\cdot}65$ s. From the first trace in this figure, depicting the wavemaker displacement, one sees that initially the wavemaker was generating a uniform wavetrain. Subsequently, the modulation was turned on for a period of about 6 min, after which the modulation was again turned off. The second trace shows the upper interfacial wave form, and the third trace shows the internal displacement of the lower interface. Finally, the last trace presents the lower interfacial data after it has been amplified and low-pass filtered to eliminate the carrier wave frequency. From these data, one can clearly see that initially, during the period of time when only a uniform wavetrain was being generated, the lower interfacial signal simply represented the forced response to the wave on the upper interface at the carrier wave frequency. Once the modulation is turned on, however, a low-frequency wave is generated on the lower interface by the spatial inhomogeneity of the carrier wave envelope. This lower interface wave has the frequency of, and is phase-locked to, the modulation. When the modulation is removed, this component of the lower-layer signal disappears.

On the basis of the theoretical discussion presented in § 2, one anticipates that the magnitude of the lower interfacial wave resulting from this resonant coupling should scale with the magnitude of the short-wave envelope spatial inhomogeneity. This is demonstrated in figure 15 where one finds that a doubling of the modulation amplitude, keeping the short-wave peak-to-peak amplitude fixed, results roughly in a doubling of the long-wave amplitude.

Figure 16 shows the result of a single-pulse experiment. Here one finds that an initial burst of high-frequency internal-wave energy can result in the production of a single, well-defined low-frequency wave. The shape of this long-wave component has the same general appearance as that of the derivative of the short-wave envelope; a result which may be anticipated from the resonance equations. Figure 17 shows the

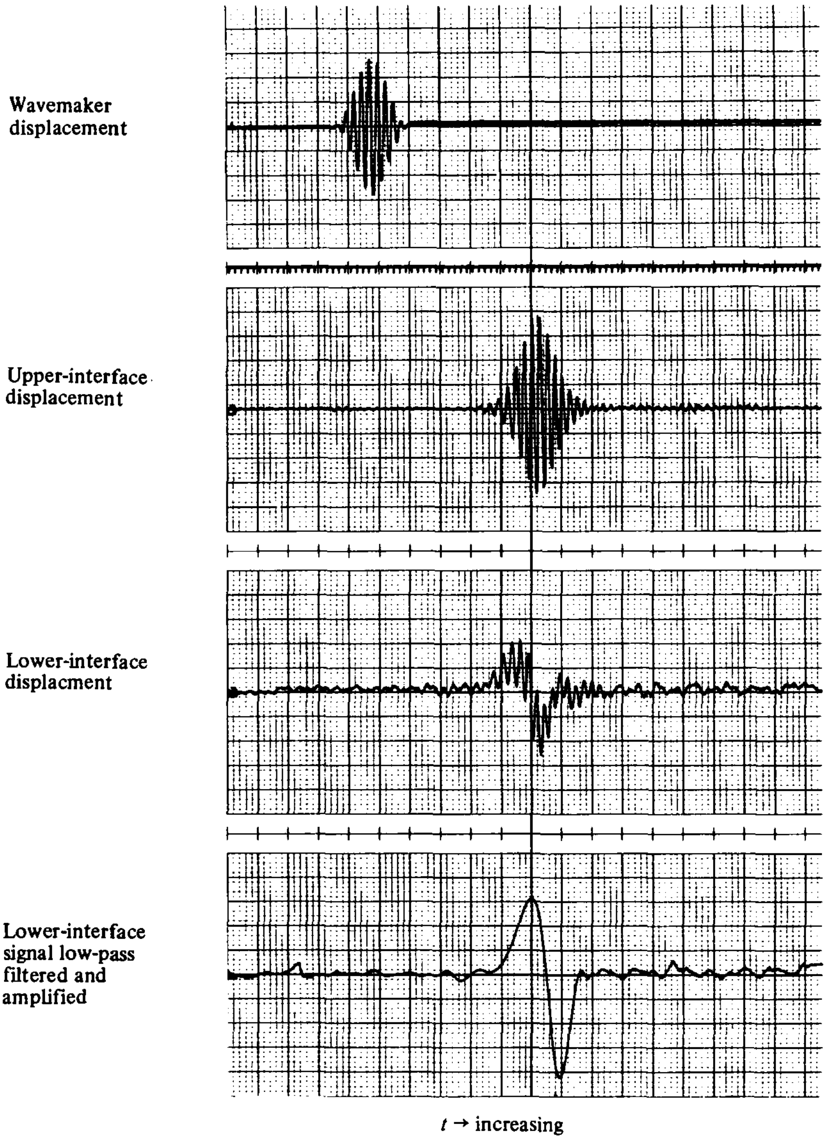

FIGURE 16. Example of a single-pulse experiment.

results of a similar experiment, except that in this situation the modulation is a negative pulse (sometimes called a 'dark pulse'). As anticipated from the theory, one finds that the character of the long wave generated by this short-wave envelope is similar to that of the previous pulsed experiment, except that the sign of the long wave is reversed.

Finally, figure 18 presents a case where the roles of the mode 1 and mode 2 disturbances are reversed. In the previous examples, energy transfer has been predominantly in one direction, proceeding from the modulated carrier wave to the lower interfacial long wave. Figure 18 demonstrates, though, that this interaction can also proceed in the opposite direction. In this configuration (shown schematically

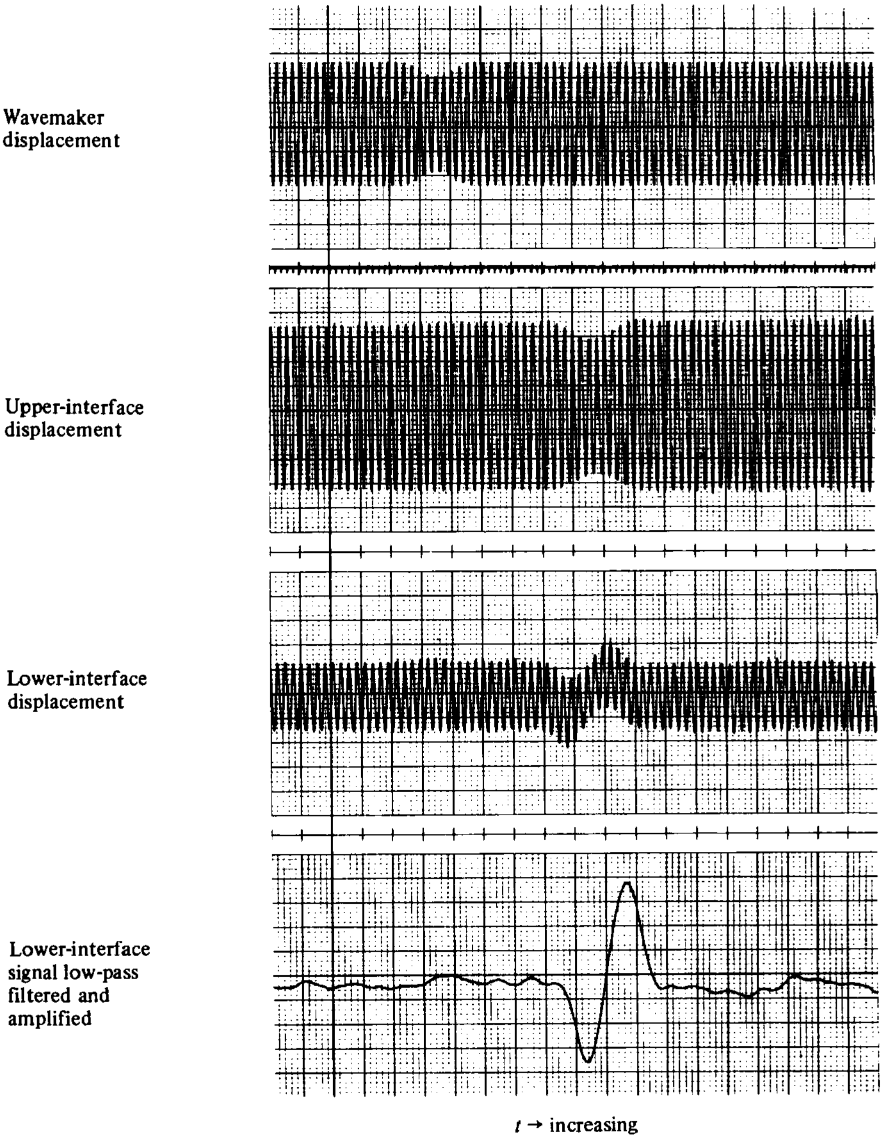

FIGURE 17. Example of a 'dark-pulse' experiment.

in figure 10*b*) a pre-existing long wave (produced mechanically, rather than hydrodynamically) acts to generate modulations in an initially uniform carrier wave. This type of behaviour is quite similar to the internal-wave/surface-wave interaction studied by Lewis, Lake & Ko (1974). Figures 14 and 18 suggest, at least qualitatively, how the resonant interchange of energy between the mode 1 and mode 2 waves may oscillate on a time scale which is long relative to the modulation time. Conceptually, what one might expect is that an initially modulated short wave acts to feed energy into the production of a long-wave component. Eventually, the energy contained in the long wave grows to a significant fraction of the carrier wave energy. At this point, the energy flow reverses through the detuning effect that the long wave has on the

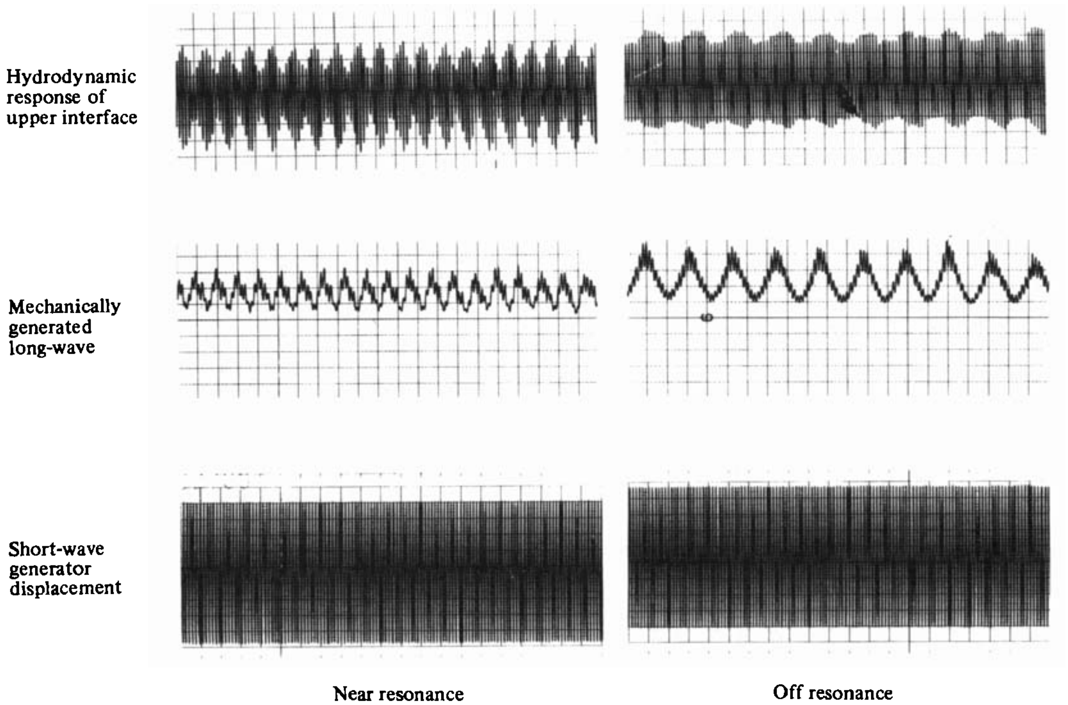

FIGURE 18. Modulation of a uniform carrier wave by a pre-existing long wave.

carrier wave. The numerical solutions previously presented (figure 6) clearly show that the long-wave/short-wave interaction equations admit solutions exhibiting such recurrence.

In summary, the qualitative results presented in this section demonstrate:

(*a*) mode-2 long-wave generation is dependent upon spatial gradients of the mode-1 carrier-wave envelope;

(*b*) larger modulations in the carrier-wave envelope produce larger-amplitude mode-2 waves;

(*c*) a single burst of high-frequency energy can produce a single, well-defined wave;

(*d*) the interaction may proceed in either of two ways, *viz*. energy transfer from a modulated short wave to the long wave as well as energy transfer from a pre-existing long wave to a mode-1 carrier wave;

3.4. *Long-wave/short-wave interaction; quantitative results*

In the previous section we have presented evidence which demonstrates in a qualitative fashion how many of the important features of the long-wave/short-wave resonant interaction anticipated from the theory are experimentally observed. The degree to which this theory is quantitatively correct is the subject of the present section. As previously described, the procedure followed was to generate mechanically a modulated wavetrain on the upper interface, and observe the resulting hydrodynamic response of the lower layer. Measurements were made for 12 min intervals on the channel centre-line at 16 longitudinal positions for each of the 9 test cases identified in table 1.

For each 12-minute data record the long-wave amplitude was determined by playing

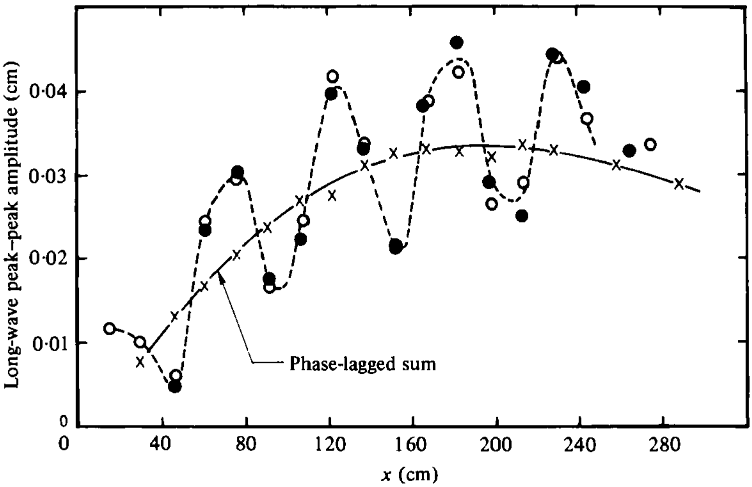

FIGURE 19. Phase-lagged sum (PLS) data for $T_{\mathrm{SW}} = 1{\cdot}3$ s. ○, probe 11; ●, probe 21; ×, phase-lagged sum.

the tape-recorded signal from probe 11 (or 21) into a spectrum analyser† and integrating the power in the neighbourhood of the long-wave frequency.

Using spectral measurements, we investigated the spatial evolution of the long-wave component as a function of the longitudinal co-ordinate for each of the nine test conditions. The results for $T_{\mathrm{SW}} = 1{\cdot}3$ s are shown in figure 19, where data from both of the lower interfacial probes (11 and 21) are presented. One may recall from previous discussion (§3.1) that for a fixed position the two probe measurements are separated in time by roughly thirty minutes. Hence, a comparison of the two sets of data constitutes a good check on the repeatability and stationarity of the measurements. In examining figure 19, one may say that the two measurements show reasonably good agreement, and both tend to show that a rather well-defined standing-wave pattern exists. Based upon previous discussion regarding the partial reflection of long-wave energy off the lower interfacial wave absorber (§3.1), however, this result is not unanticipated. The problem one faces here is that in order to study the long-wave/short-wave resonant interaction, it is necessary to discriminate between the wave propagating *downstream* (which is receiving energy from the modulated carrier wave) and the *upstream* propagating wave (which reflected off the wave absorber and is slowly decaying under the action of viscosity). This discrimination between the two waves was partially accomplished in the following manner. The lower interfacial IR probes are longitudinally displaced by 29·85 cm. The wavelength of a free wave on the lower interface having a period equal to that of the modulation is 118·4 cm. Assuming that the standing-wave pattern observed in figure 19 is generated by the linear superposition of two waves propagating in opposite directions, the long-wave component of the lower interfacial displacement field, $\eta_{\mathrm{LW}}(x,t)$, may be represented by the expression

$$\eta_{\mathrm{LW}}(x,t) = a_1 \cos(k_{\mathrm{LW}}x - \omega_{\mathrm{LW}}t) + a_2 \cos(k_{\mathrm{LW}}x + \omega_{\mathrm{LW}}t + \phi),$$

---

† The particular spectrum analyser used (Rockland, model FFT 512/S) had the capability of digitally integrating the area under the spectrum between any two arbitrarily determined frequencies.

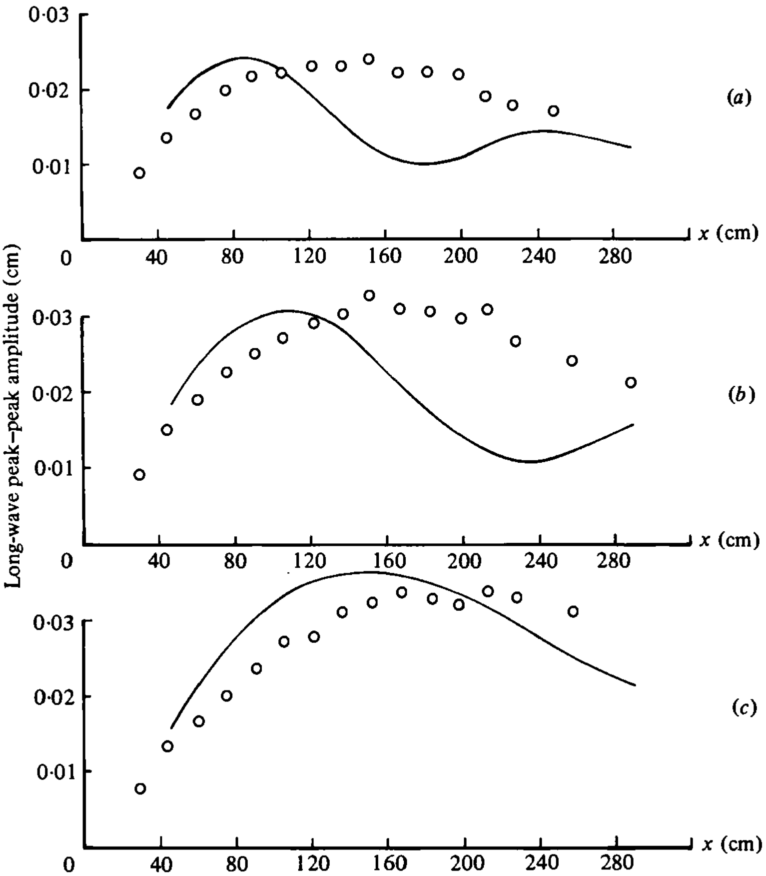

FIGURE 20. Comparison of the phase-lagged-sum measurements with the numerically computed evolution of the long-wave component. (a) $T_{sw} = 1{\cdot}1$ s; (b) $T_{sw} = 1{\cdot}2$ s; (c) $T_{sw} = 1{\cdot}3$ s; (d) $T_{sw} = 1{\cdot}4$ s; (e) $T_{sw} = 1{\cdot}4$ s; (f) $T_{sw} = 1{\cdot}63$ s; (g) $T_{sw} = 1{\cdot}7$ s; (h) $T_{sw} = 1{\cdot}8$ s; (i) $T_{sw} = 1{\cdot}9$ s. ○, data; ——, computed.

where a_1 and a_2 are the downstream and upstream propagating wave amplitudes respectively, k_{LW} and ω_{LW} are the long-wave wavenumber and frequency, and ϕ is an arbitrary phase. Using this representation the signals from probes 1l and 2l (separated by $\pi/2k_{\mathrm{LW}}$) are given by

$$\eta_{1l}(t) = \eta(x_0, t),$$

$$\eta_{2l}(t) = \eta(x_0 + \pi/2k_{\mathrm{LW}}, t),$$

when $\eta_{1l}(t)$ and $\eta_{2l}(t)$ are the signals from the respective probes. If we now define an operation whereby the signal from probe 1l is phase-lagged in time by an amount $\pi/2\omega_{\mathrm{LW}}$ and added to the output of probe 2l (and dividing by 2) we obtain

$$\tfrac{1}{2}\{\eta_{1l}(t - \pi/2\omega_{\mathrm{LW}}) + \eta_{2l}(t)\} = a_1 \cos(k_{\mathrm{LW}} x_0 - \omega_{\mathrm{LW}} t + \tfrac{1}{2}\pi),$$

which is simply the *downstream* propagating wave phase shifted by $\pi/2$. Thus, the above operation (which for lack of a better name will be termed the phase-lagged sum or PLS) acts as a discriminator, and picks out that portion of the record which

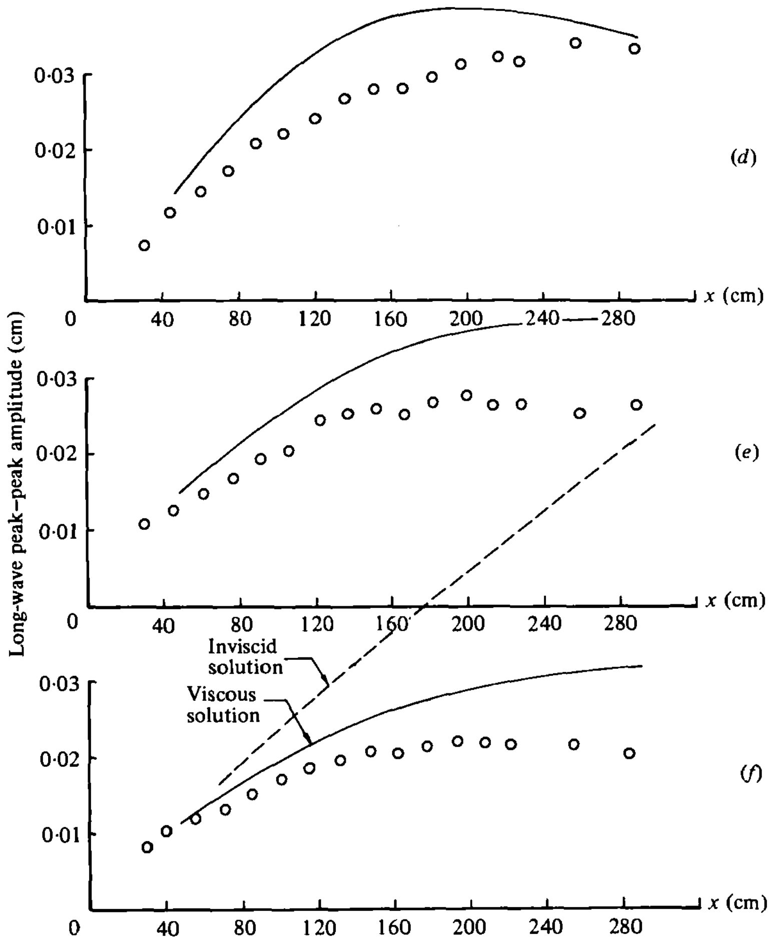

FIGURE 20 (*d–f*). For legend see p. 393.

corresponds to a downstream propagating wave. Figure 19 presents a comparison between the individual probe measurements and the PLS results. In examining these two sets of data, one finds that the PLS technique virtually eliminates the standing-wave pattern, and describes the spatial evolution of a long-wave component which is growing with longitudinal co-ordinate due to its interaction with the short-wave modulation.

The PLS data for all of the experimental conditions are shown in figure 20. The solid curve through each data set represents the theoretical result which will be subsequently discussed. One observes from the experimental measurements that the spatial growth rate of the long-wave component is a strong function of the short-wave frequency, with larger initial growth rates occurring at smaller values of T_{SW}. One also notes from these data that the long-wave amplitude does not monotonically increase with x, but rather appears to grow to a maximum and subsequently decay. This non-monotonicity in the long-wave component was not understood initially. One possibility considered was whether or not this decline in the long-wave amplitude was indicative of the transfer of energy from the mode-2 wave back into the mode-1

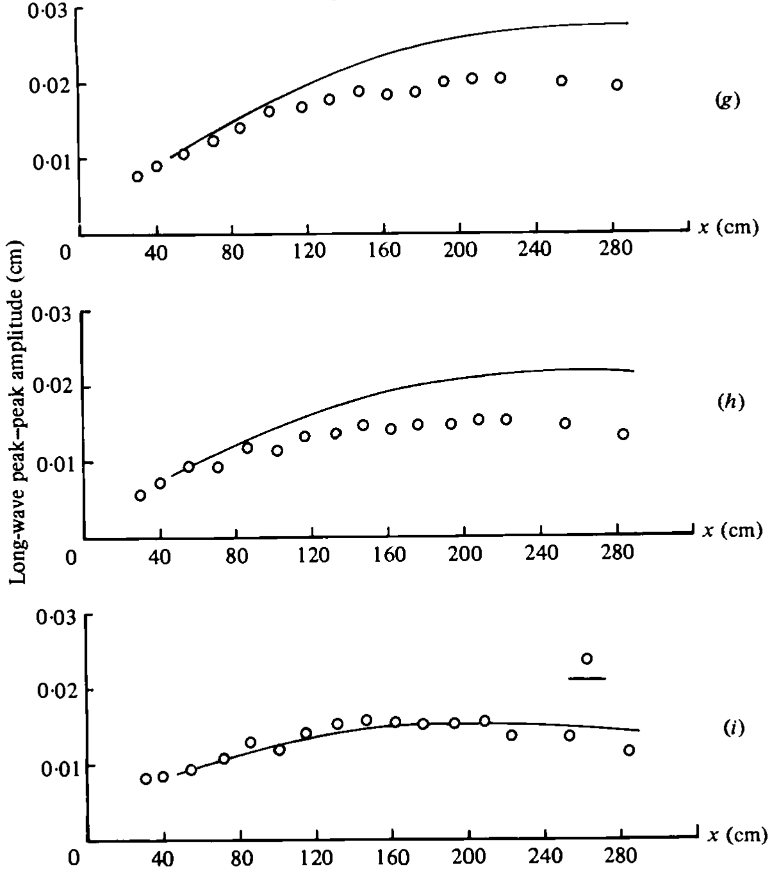

FIGURE 20 (g–i). For legend see p. 393.

carrier wave. However, using numerical solutions to the resonant interaction equations with an *ad hoc* viscous damping term, we believe that the observed attenuation in the long-wave component is primarily due to the viscous dissipation. Further discussion of these numerical results is deferred to the next section.

Using the PLS measurements of figure 20, one may determine the magnitude of the initial growth rate of the long wave by calculating the derivative of a least-squares curve used to fit the data, evaluated at $x = 30$ cm (i.e. the first measurement station). The results are shown in figure 21 (a) as a function of the carrier wave period. It is interesting to note here that the initial growth rate of the long-wave mode is not maximized at the resonant condition, but rather one finds larger growth rates at the higher frequencies. The reason for this somewhat non-intuitive result is discussed in the next section. Figure 21 (b) presents the maximum observed long-wave amplitude as a function of the short-wave period.

Another measurement of interest in this investigation of the long-wave/short-wave resonant interaction is the phase relationship which exists between the short-wave modulation envelope and the long wave. This relationship was measured by cross-correlating the modulation envelope† with the lower interfacial PLS signal, and

---

† The modulation envelope was obtained by squaring the upper interfacial signal and low-pass filtering. Extreme care was taken to account for phase shifts introduced by the filter.

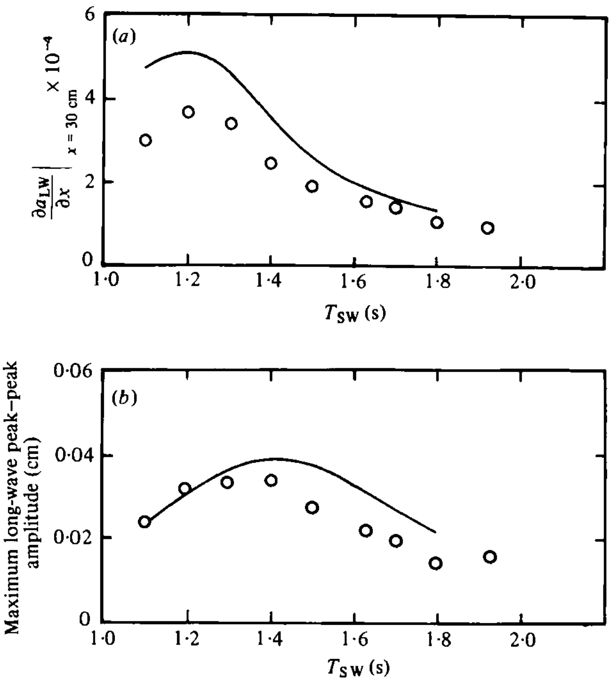

FIGURE 21. Comparison of (*a*) the measured spatial growth rate and (*b*) the maximum long-wave amplitude with theoretical predictions. ○, data; ——, theory.

measuring the time delay for maximum correlation. Figure 22 shows the results of this measurement for all of the test conditions. Here, the phase Φ is defined relative to the short-wave envelope such that, for $0 < \Phi < 180^\circ$, the long wave *leads*, and for $-180^\circ < \Phi < 0^\circ$ the long wave *lags* the modulation. At the resonant condition, $T_{SW} = 1\cdot63$ s, the initial long-wave/short-wave phase relationship is roughly 112° with the long wave leading the modulation. This phase orientation is approximately maintained throughout the interaction. For $T_{SW} > 1\cdot63$ s, the long wave lags the modulation by an ever increasing amount during the interaction, indicating that the modulation is propagating faster than the long wave. This result is not unanticipated, since for these cases $C_{LW} < C_{gSW}$. As one would expect, for $T_{SW} < 1\cdot63$ s, the reverse trend is observed. These results are useful, in that they demonstrate how only at resonance is the phase relationship between the short-wave envelope and the long wave unchanged during the duration of the interaction. For off-resonant conditions, the initial phase orientation is continuously altered during the interaction, due to the mismatch in the short-wave group and the long-wave phase speeds.

3.5. *Comparison of theory and experiment*

Before proceeding to a discussion of the comparison of the theoretical predictions with the experimental data, it is first necessary to discuss how the effects of viscosity may be incorporated into the present inviscid model. We have previously demonstrated (§3.2) that viscosity can have an important influence upon the amplitude of the short-wave mode, particularly for the higher-frequency waves. A non-negligible amount of dissipation also occurs for the long waves on the lower interface. Clearly,

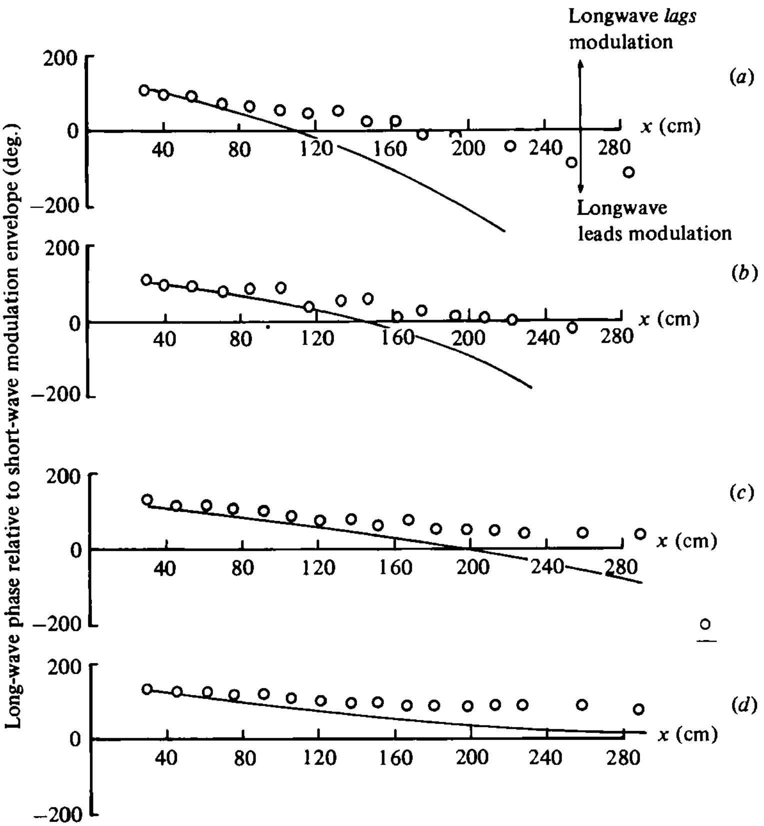

FIGURE 22. Comparison of measured and computed phase relationship between the long-wave and the short-wave modulation envelope. (*a*) $T_{SW} = 1{\cdot}1$ s; (*b*) $T_{SW} = 1{\cdot}2$ s; (*c*) $T_{SW} = 1{\cdot}3$ s; (*d*) $T_{SW} = 1{\cdot}4$ s; (*e*) $T_{SW} = 1{\cdot}5$ s; (*f*) $T_{SW} = 1{\cdot}63$ s; (*g*) $T_{SW} = 1{\cdot}7$ s; (*h*) $T_{SW}) = 1{\cdot}8$ s; (*i*) $T_{SW} = 1{\cdot}925$ s. ○, data; ——, computed.

if detailed quantitative comparisons are to be made between the theory and experiment, some attempt must be made to incorporate viscosity into the analytical model. This has been accomplished, albeit in an *ad hoc* fashion, by simply adding a viscous dissipation term with an empirically determined dissipation constant to each of the evolution equations. These modified equations are written as:

$$iS_\tau + \lambda S_{\xi\xi} = \nu_1 LS - D_s S, \tag{3.1}$$

$$L_\tau + C_0 \Delta L_\xi = \alpha'(|S|^2)_\xi - D_L L, \tag{3.2}$$

where

$$\xi = \epsilon^{\frac{2}{3}}(x - C_g t), \quad \tau = \epsilon^{\frac{4}{3}} t,$$

and

$$\alpha' = \frac{\alpha}{C_g(C_g + C_{23})(C_g^2 - C_{12}^2)}, \quad \Delta = \frac{C_0 - C_g}{\epsilon^{\frac{2}{3}} C_0}.$$

In the absence of modal interactions (i.e. $\nu = \alpha = 0$), these equations simply describe waves which are exponentially decaying due to the effects of viscosity. One note of caution which should be made here is that this viscous model is purely *ad hoc*. No attempt has been made to determine whether viscosity has any effects other than

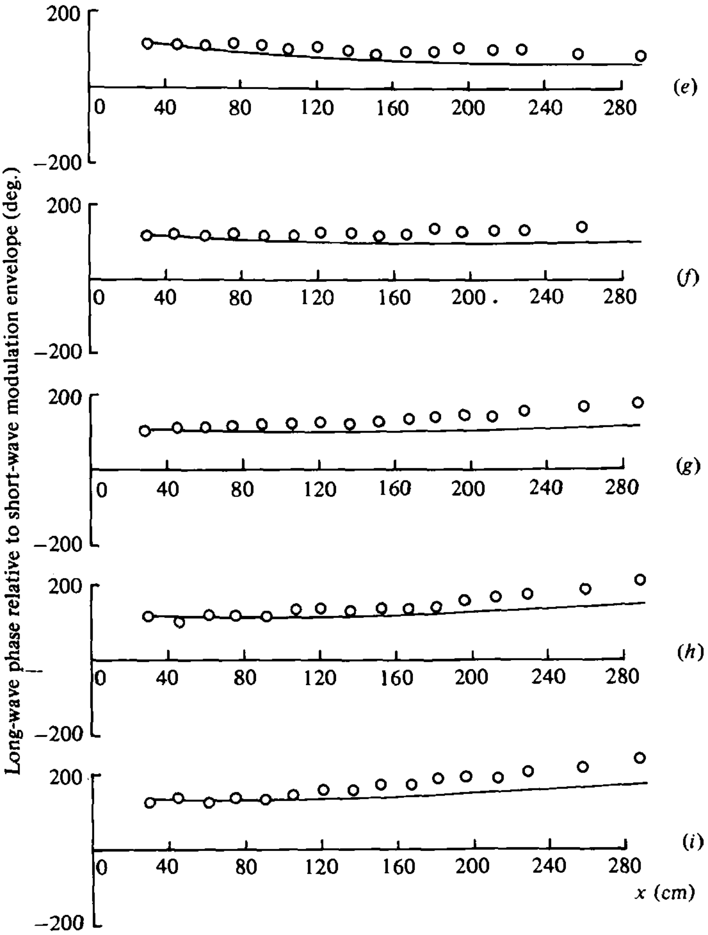

FIGURE 22 (e–i). For legend see p. 397.

pure amplitude attenuation which might be important during the interaction. These might include a viscous modification to the dispersion relation which would alter all of the coefficients, or boundary-layer effects which might alter the values of the coupling coefficients (which are essentially integrals of inviscid eigenfunctions).

For the purpose of comparison with the data, equations (3.1) and (3.2) were solved numerically using the time-stepping leap-frog technique discussed by Fornberg (1977). The initial conditions for these calculations included the measured short-wave and long-wave amplitudes at $x = 30$ cm (i.e. the first measurement station) as well as the initial phase relationship between the long-wave and the short-wave modulation envelope.

The single most important result of the long-wave/short-wave analysis outlined in §3 and detailed in the appendix is the determination of the nonlinear coefficients ν_1 and α' which appear in equations (3.1) and (3.2), respectively. For the present experimental configuration these coefficients have been evaluated, and their functional dependence upon the short-wave period T_{SW} is shown (in dimensional form) in figure 23. For the present experiment, the coefficient in the long-wave equation is of greater importance, and hence we will focus our attention upon this quantity.

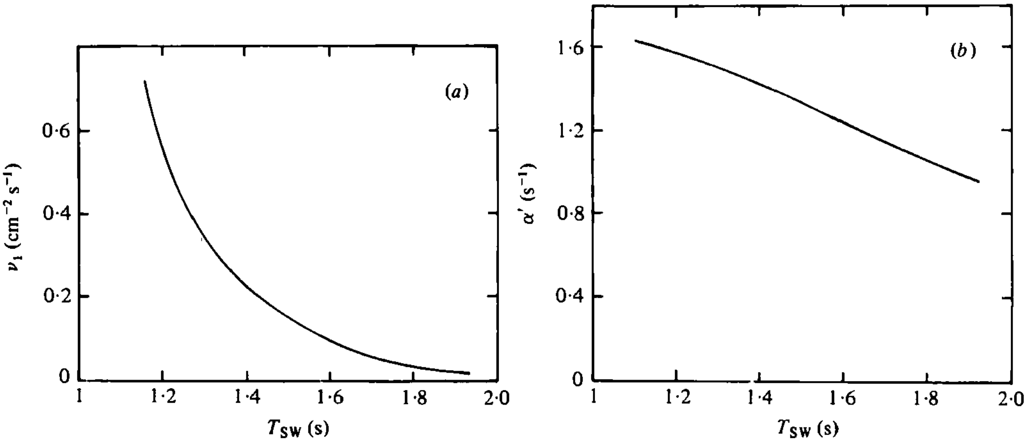

FIGURE 23. Coupling coefficients (*a*) ν_1 and (*b*) α' which appear in the short-wave and long-wave evolution equations, (3.1) and (3.2) respectively, versus T_{SW}.

Essentially, the coefficient α' measures the amplitude of the long wave or mean-flow portion of the upper interfacial wavefield which exists due to the slightly nonlinear nature of the short-wave wavetrain. In a sense, the term $\alpha'(|S|^2)_\xi$ which appears on the right-hand side of the long-wave equation is not directly related to resonance, but merely represents (at least initially) a forcing term in the equation which arises due to the mean flow portion of the short wave. The concept of 'resonance' enters when the propagation speed for this mean flow component (which is bound to the short wave, and hence propagates at the short-wave group velocity) matches the long-wave phase velocity of some other mode; i.e. $C_g = C_0$. When this occurs, the long-wave forcing function $\alpha'(|S|^2)_\xi$ propagates at the same speed as the higher-mode long wave, and significant energy transport into this higher mode may be expected. At resonance, one anticipates that a particular phase orientation shall exist between the long wave and the envelope of the short-wave modulation such that the growth rate is maximized. For off-resonance conditions, however, this preferred phase orientation cannot be maintained, since the forcing term and the long wave propagate at different speeds. This lack of phase stationarity will have a destructive influence upon the strength of the interaction.

With these concepts in mind, we may discuss (at least qualitatively) what one would expect to observe experimentally as the period of the short wave is varied. At the resonant condition ($T_{SW} = 1{\cdot}63$ s), where $C_g = C_0$, one anticipates that the long-wave component will grow initially at the expense of the short-wave mode, and that a fixed phase relationship will be maintained between the long wave and the short-wave modulation envelope. From an examination of the long-wave equation, one concludes that (for $\alpha' > 0$) at resonance the peak in the long wave should lag the peak in the short-wave modulation envelope by 90°.

As one moves away from resonance, say towards smaller short-wave periods, several changes occur. First, one notes from figure 23 that as T_{SW} decreases α' increases. This simply implies that the mean flow part of the short-wave wavefield is larger at higher carrier-wave frequencies (essentially, the wave becomes more nonlinear since increasing the frequency increases the maximum wave slope). A second effect which occurs as one moves away from resonance is related to the change in the group velocity. One recalls that the experiments were performed in such a manner that the period of the modulation was held fixed between the nine test cases. However, as one decreases the short-wave period, one also decreases the group velocity, which decreases the *wavelength* of the modulation, and hence increases the magnitude of the spatial gradients of the modulation envelope. Since the long-wave interaction is being driven by these spatial gradients, a decrease in the short-wave period may actually result in an increase in the strength of the interaction. Combining the effects of these two processes, one arrives at the somewhat non-intuitive conclusion, that stronger interactions might occur at off-resonant conditions. However, this result cannot be true indefinitely, for, as one moves very far away from resonance, the mismatch between the group and phase speeds also becomes large, and this will have a destructive effect upon the interaction. Furthermore, as T_{SW} approaches zero the short waves must approach the deep water limit, and as shown by Djordjevic & Redekopp (1977), the coefficient α' must go to zero. Hence, one concludes that, as T_{SW} moves away from resonance towards smaller wave periods, the strength of the interaction may initially increase, but for far off-resonant conditions the interaction strength must ultimately diminish.

On the other side of resonance (i.e. $T_{\mathrm{SW}} > 1{\cdot}63$ s) α' decreases, the magnitude of the gradient of the modulation decreases, and the mismatch in the group and long-wave phase speed increases. The net combined effect of all of these processes is to diminish the strength of the interaction.

The numerical solutions for the nine experimental test conditions, $1{\cdot}1 \leqslant T_{\mathrm{SW}} \leqslant 1{\cdot}925$ s, are presented in figures 20 and 22 as a function of longitudinal co-ordinate (time has been converted to distance using a group velocity transformation). In figure 20, the calculated evolution of the maximum peak–peak amplitude of the long wave on the lower interface is presented. Figure 22 presents the corresponding calculations of the relative phase orientation between the long-wave and the short-wave modulation envelope. The convention adopted in these calculations is that a positive phase corresponds to the long-wave lagging the short-wave modulation. To facilitate direct comparison with the data, the long-wave amplitude computed in the program corresponds to the phase-lag-sum (PLS) definition described in §3.4. Several comments may be made regarding the results presented in these figures.

For $T_{\mathrm{SW}} = 1{\cdot}1$ s one observes in figure 20 that the initial growth rate of the computed long-wave amplitude is greater than what is observed in the experiment. At about $x = 80$ cm, this long-wave amplitude is maximized and subsequently decreases. At $x \simeq 180$ cm a curious phenomenon occurs: the computed long wave once again starts to increase, achieves a maximum at $x \simeq 250$ cm, and again decreases. The calculations for the case $T_{\mathrm{SW}} = 1{\cdot}2$ s reveal the same qualitative behaviour, although the period of oscillation for this run is somewhat greater. None of this periodic structure is observed in the data. Examination of the computed phase relationships shown in figure 22 reveals the probable cause for this oscillatory behaviour of the long-wave amplitude. Initially, the phase orientation between the long wave and the short-wave modulation is 118° (the long wave *lagging* the short wave), which is close to the 90° phase relation most conducive for growth. However, because the mismatch between the group and phase speeds is so large for this case, this phase orientation changes rapidly. By $x = 110$ cm, the computed phase difference is 0°, and at $x = 150$ cm the long wave leads the short wave by 90°. At this location, then, the phase of the long wave has been shifted by 180° from that orientation most conducive for growth. One intuitively expects that such a phase change can only have an adverse effect upon the energy transport into the long-wave mode.

Comparing the results of the calculations in figures 20 and 22 with the experimental data for $T_{\mathrm{SW}} = 1{\cdot}1$ and $1{\cdot}2$ s, one finds that the agreement is not very good. As has been noted, the data show none of the oscillatory behaviour of the long-wave component, and the initial growth rate is less than what is theoretically predicted. Examining the phase data for these two cases, one can see that the cyclical nature of the computed results arises because the predicted rate of change of phase is significantly larger than the observed. For example, in the experiment during the growth stage of the interaction, the phase of the long wave is never shifted more than 50° from that phase orientation which maximizes the growth rate. During this same interval, however, the theory predicts phase shifts of 180° or more, which results in an attenuation of the long-wave amplitude at certain locations during the interaction. This overprediction in the rate at which the phase of long wave varies is believed to be directly related to the approximations which were made to reduce the order of the full fourth-order long-wave operator to a first-order system, as discussed in §2. As was noted there, for small deviations from resonance the approximations used to reduce the order of this operator should be valid, but for far off-resonant conditions one should solve the full fourth-order equations. Thus, even though the theoretical and experimental agreement is fairly poor for these two cases, the results are useful from the standpoint that they identify how far off resonance one may go before the first-order equations become inappropriate.

For $T_{\mathrm{SW}} \geqslant 1{\cdot}3$ s, the qualitative agreement between the theory and the experiment is better. The initial growth rate of the long wave and the evolution of the phase orientation are seen to be in closer agreement. These conclusions are also generally true for those off-resonant conditions where $T_{\mathrm{SW}} \geqslant 1{\cdot}63$ s. The theory also predicts the observed equilibration of the long-wave amplitude at some maximum value after the initial growth stage, although the actual amplitude at this point is overestimated in the theory by as much as 50 %. However, the fact that the program predicts this long-wave equilibration at all is in itself an important result. Initially, the observed non-monotonic behaviour of the long-wave amplitude was not understood. It was believed, for example, that the long-wave growth should persist for the entire length of the test section. Several possible explanations were explored, but from the numerical scheme it is almost certain that this equilibration in the long-wave amplitude is primarily due to viscous effects. Consider, for example, the data for the case $T_{\mathrm{SW}} = 1{\cdot}63$ s. In addition to the previously discussed calculations, a second numerical run was made with the viscous terms in equations (3.1) and (3.2) set equal to zero. The results, which are shown by the dashed line in figure 20, demonstrate that in the absence of viscosity the long wave continues to extract energy from the short-wave modulation over the entire range of x in which measurements were made. The inclusion of viscosity dramatically alters the character of the solution, and the results are more consistent with the data.

Because the viscous terms are so important in the later stages of the interaction, one has to question whether the *ad hoc* viscous model used in the numerical scheme is really adequate accurately to describe the long-wave maximum-amplitude state. It is quite possible, for example, that the over-prediction of the maximum long-wave amplitude by the numerical code is not a reflection of an inadequacy in the long-wave/short-wave resonance theory, but rather due to our attempts to modify the analysis to include viscous effects. However, development of a more complete theory which incorporates viscosity into the problem at the outset is a formidable task, and such an analysis is not forthcoming in the foreseeable future.

Some of the important features of the experimental and theoretical results shown in figure 20 are summarized in figure 21. The predicted initial growth rates of the long wave are presented as a function of the short-wave period in figure 21 (*a*). The experimental results are also shown here. The results are interesting in that much of the anticipated qualitative behaviour of the initial growth rate is corroborated. For example, at the resonance condition the computed long-wave growth rate is $1{\cdot}77 \times 10^{-4}$ cm/cm. As T_{SW} decreases, the growth rate increases due to the combined effect of the coefficient α' increasing and the modulation wavelength decreasing. This trend continues until $T_{\mathrm{SW}} = 1{\cdot}2$ s. However, at $T_{\mathrm{SW}} = 1.1$ s, both the theoretical and experimental growth rates are smaller, indicating that the mismatch in C_g and C_0 has become sufficiently large to diminish the effectiveness of the interaction. For $T_{\mathrm{SW}} > 1{\cdot}63$ s, α' decreases, the modulation wavelength increases and $(C_0 - C_g)$ increases, so that, as expected, the growth rate monotonically decreases. Comparing the theory with the experimental results, one finds good qualitative agreement especially when one notes that both predict a maximum in the long-wave growth rate at $T_{\mathrm{SW}} = 1{\cdot}2$ s. The quantitative agreement is fairly good around resonance, but gets progressively worse as T_{SW} decreases. As previously noted, however, this is probably due to the approximations made in reducing the order of the long-wave equation.

Figure 21 (*b*) summarizes the maximum amplitude state of the long wave as a function of the short-wave period. Again, there is fairly good qualitative agreement with the data, although in general the theory tends to overpredict the maximum amplitude. The degree to which these results would be modified by a more complete viscous theory is not known at present.

Another piece of information which is worth discussing is the degree to which the present analytical model may be used to choose a suitable normalization such that all of the data may be plotted in some universal form. We know, for example, that at resonance the form of the inviscid long-wave evolution equation is given by

$$\frac{\partial L}{\partial t} = \alpha'(|S|^2)_\xi,$$

where

$$S(\xi, t = 0) = \frac{a_{\mathrm{SW}}}{4}\left[1 + \frac{a_{\mathrm{mod}}}{a_{\mathrm{SW}}}\cos\frac{2\pi\xi}{\lambda_{\mathrm{mod}}}\right]$$

with a_{SW} being the short-wave peak–peak amplitude, a_{mod} the modulation amplitude, and λ_{mod} the modulation wavelength.

Thus, for $a_{\mathrm{mod}}/a_{\mathrm{SW}} \leqslant 1$, the natural scaling for the interaction should be given by

$$\bar{a}_{\mathrm{LW}} = \frac{a_{\mathrm{LW}}}{\frac{1}{2}\pi a_{\mathrm{SW}}\, a_{\mathrm{mod}}\,\alpha'/C_g}, \quad \bar{x} = x/\lambda_{\mathrm{mod}}.$$

Figure 24 (*a*) shows the initial unscaled data, plotted over the range of x where the long-wave growth is fairly linear. In figure 24 (*b*), these data are plotted in normalized

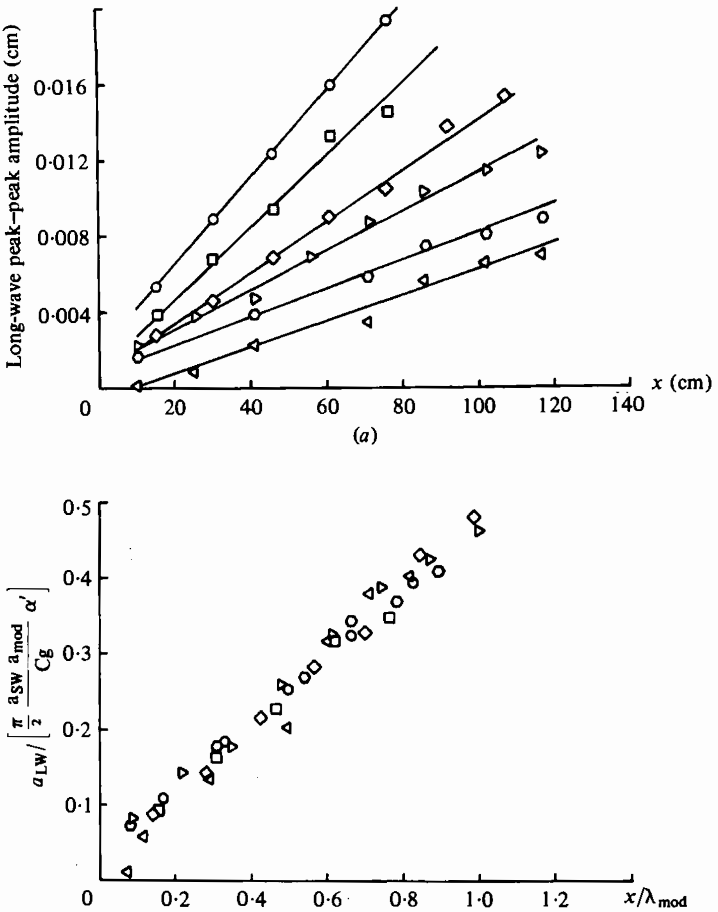

FIGURE 24. Comparison of (*a*) raw data with (*b*) normalized data. The normalization is predicted by the theory. T_{SW} (s); ○, 1·3; □, 1·4; ◇, 1·5; ▷, 1·63; ○, 1·8; ◁, 1·925.

co-ordinates, and one sees that the above normalization does indeed collapse the data to a single curve. It is worth pointing out here, that this form of normalization is more than just dimensional analysis, since the coefficient α' which appears in the denominator is a function of T_{SW}, and must be computed for each set of data.

One final piece of information which is worth while presenting, deals with the effects of viscosity upon the evolution of the interaction. In most of the calculations thus far presented, the various constants which appear in the equations have been chosen to simulate the experimental test conditions. One wonders, however, how the interaction would proceed in an inviscid fluid, where, due to the lack of dissipation, the interaction could persist for distances which are unachievable in the laboratory. Figure 25 presents one calculation made for an inviscid fluid. The system was assumed to be at resonance, and the calculation was carried out over a propagation distance of some 36 m. Also shown here is the viscous calculation carried out to 2·8 m. In examining the results shown in this figure, one is forced to conclude that in the present experiment only the very earliest stages of the interaction are capable of being investigated. Unfortunately, most of the interesting phenomena and the largest amounts of modal

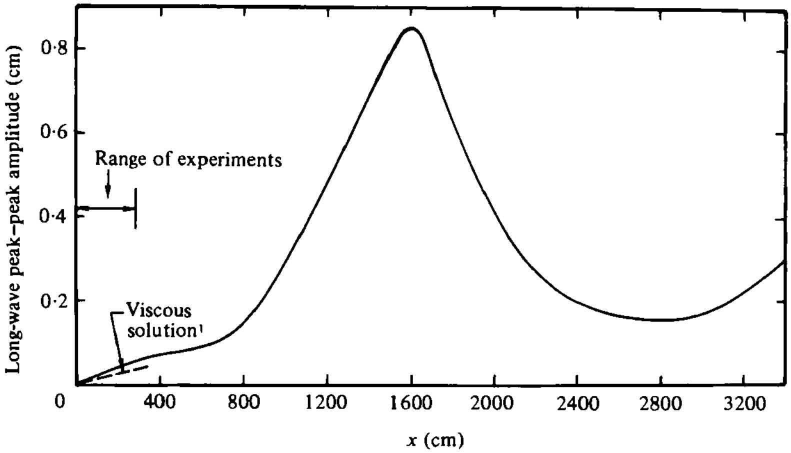

FIGURE 25. Inviscid numerical calculation carried out to investigate long-time evolution of the long-wave component. $T_{SW} = 1{\cdot}63$ s.

energy transport occur at interaction distances far removed from what may be experimentally studied. It is interesting to note from this calculation, though, that some periodicity exists in the energy transfer to the long wave, with a wavelength of roughly 28 m. However, for the particular initial conditions imposed in this calculation, perfect recurrence was not observed.

4. Summary

The analytical and experimental study which has been presented in this report has identified several aspects of internal wave propagation which arise due to nonlinear processes. The nonlinear Schrödinger equation, which has been shown to govern the evolution of a weakly nonlinear internal wave mode, becomes singular when certain resonant criteria are satisfied. In one situation, a resonance was shown to be possible between the short-wave mode and a long wave of higher mode number. When these conditions occur, the problem must be reformulated, and the relevant description of the wavefield was shown to be governed by the so-called long-wave/short-wave resonant interaction equations.

In general, the theorectical predictions are in qualitative agreement with the experimental results, particularly in regard to the ability of a modulated short-wave mode to transfer energy to a higher-mode long wave. The quantitative agreement between the theory and the experiment is in most cases reasonably good, although complications existed in making comparisons. These difficulties include trying to incorporate the effects of viscosity into an inviscid theory, and approximating a fourth-order partial differential equation by one which is first order, in order to facilitate the numerical solution. In general, however, we feel that the analytical theory has been reasonably validated by direct experimental comparison.

The application of this resonant interaction theory to motions of geophysical interest are numerous. In the ocean, for example, it is widely known that the ambient internal wave field is dominated by longer wavelength low-frequency components with the majority of the energy lying within a few octaves of the local inertial frequency. Energy in the short-wave modes will almost certainly be dynamically coupled to the long-wave ambient background through which it propagates. The time scales required for significant interaction to occur in general are not easily estimated, and direct numerical evaluation of the coupling coefficients in the resonant interaction equations for a given stratification is required. It is anticipated, however, that, because these coupling coefficients involve *derivatives* of the eigenfunctions and the Brunt–Väisälä distribution, in a highly structured stratification (which characterizes much of the ambient ocean) the magnitude of these coefficients might be sufficiently large as to require the inclusion of this resonant mechanism for an accurate description of the wavefield. Similar statements may be made regarding atmospheric wave motions.

The authors acknowledge the assistance of Dr B. M. Lake and Dr C. L. Hindman who participated in several helpful discussions regarding this work. We are also indebted to Mr D. Rowland for his assistance in building the experimental apparatus and, most importantly, making it work.

This study was sponsored by the Applied Physics Laboratory of the Johns Hopkins University under contract APL/JHU no. 601038.

Appendix

In this appendix we study the interaction of a short and long internal wave propagating in a system comprised of three homogeneous layers having different density. This configuration is shown schematically in figure 9(*a*).

The equation of motion in each layer is Laplace's equation

$$\nabla^2\phi_i = 0, \quad i = 1, 2, 3, \tag{A 1}$$

where ϕ is the velocity potential. The boundary conditions to be applied are zero vertical velocity at the solid boundaries as well as the normal kinematic and dynamic boundary conditions at the two fluid interfaces.

The displacement of the lower interface, with equilibrium position $z = 0$, is denoted by $z = \eta(x, t)$, and that of the upper interface, with equilibrium position $z = h_2$, by $z = h_2 + \zeta(x, t)$.

To construct the solution in the context of weak nonlinearities, we introduce the slow space and time scales

$$X = \mu x, \quad T = \mu t,$$

and expand the dependent variables in the manner

$$\phi_i = \delta\Phi_i(X, z, T) + \epsilon\{\phi_i^{(1)}(X, z, T)\,E + \phi_i^{(1)*}E^{-1}\} + \epsilon^2\{\phi_i^{(2)}(X, z, T)\,E^2 + \phi_i^{(2)*}E^{-2}\} + \ldots, \tag{A 2a}$$

$$\zeta = \mu\delta\, Z(X, T) + \epsilon\{\zeta^{(1)}(X, T)\,E + \zeta^{(1)*}E^{-1}\} + \epsilon^2\{\zeta^{(2)}(X, T)\,E^2 + \zeta^{(2)*}E^{-2}\} + \ldots, \tag{A 2b}$$

$$\eta = \mu\delta\, N(X, T) + \epsilon\{\eta^{(1)}(X, T)\,E + \eta^{(1)*}E^{-1}\} + \epsilon^2\{\eta^{(2)}(X, T)\,E^2 + \eta^{(2)*}E^{-2}\} + \ldots, \tag{A 2c}$$

where

$$E = \exp i(kx - \omega t).$$

In these expressions k and ω are the wavenumber and frequency of the short-wave mode with non-dimensional amplitude ϵ; μ^{-1} is a measure of the wavelength of the long-wave mode and also the modulational length scale for the short-wave mode, and

$\mu\delta$ is the amplitude of the long-wave mode. The relative magnitudes of the three small parameters μ, ϵ, δ are unspecified at this stage; the choices leading to significant interaction between the two wave modes will be made after consistent asymptotic solutions for the various dependent variables have been constructed.

Since Laplace's equation is linear, the general solution for each of the terms in (A 2*a*) can be written down without reference to the nonlinear matching conditions. The relevant solutions are

$$\Phi_i = (P_i z + Q_i) - \mu^2 \left\{\frac{z^3}{3!} P_i + \frac{z^2}{2} Q_i\right\}_{XX} + \mu^4 \left\{\frac{z^5}{5!} P_i + \frac{z^4}{4!} Q_i\right\}_{XXXX} + \dots, \tag{A 3a}$$

$$\left.\begin{aligned} \phi_i^{(1)} &= (A_i e^{kz} + B_i e^{-kz}) - i\mu z(A_i e^{kz} - B_i e^{-kz})_X - \mu^2 \frac{z^2}{2} (A_i e^{kz} + B_i e^{-kz})_{XX} + \dots, \\ \phi_i^{(2)} &= (D_i e^{2kz} + F_i e^{-2kz}) - i\mu z(D_i e^{2kz} - F_i e^{-2kz})_X - \dots. \end{aligned}\right\} \tag{A 3b}$$

Expanding the terms in the interfacial conditions in a Taylor series about the equilibrium interface positions and then substituting the asymptotic expansions (A 2) together with the solutions (A 3) into these expanded expressions and the boundary conditions yields a series of complicated expressions relating the A_i, B_i, D_i, etc., at the boundaries and across the fluid interfaces. Considering only the leading-order terms in these expressions, one obtains the dispersion relation given by:

$$\left(1 - \frac{\Omega_{12}^2}{\omega^2}\right)\left(1 - \frac{\Omega_{23}^2}{\omega^2}\right) - \frac{\rho_2 T_1}{\rho_2 T_1 + \rho_1 T_2} \frac{\rho_2 T_3}{\rho_2 T_3 + \rho_3 T_2}(1 - T_2^2) = 0, \tag{A 4}$$

where

$$\Omega_{12}^2 = \frac{gk(\rho_2 - \rho_1) T_1 T_2}{\rho_2 T_1 + \rho_1 T_2}, \quad \Omega_{23}^2 = \frac{gk(\rho_3 - \rho_2) T_2 T_3}{\rho_2 T_3 + \rho_3 T_2},$$

$$T_i = \tanh kh_i.$$

This equation is quartic in ω, the four solutions corresponding to waves travelling in both directions on both interfaces.

At next order, one obtains conditions for the long-wave terms which can be combined to yield the single long-wave equation:

$$\mathscr{L}_w f_i = \left\{(\partial_{TT}^2 - C_{12}^2 \partial_{XX}^2)(\partial_{TT}^2 - C_{23}^2 \partial_{XX}^2) - \frac{\rho_2 h_1}{\rho_2 h_1 + \rho_1 h_2} \frac{\rho_2 h_3}{\rho_2 h_3 + \rho_3 h_2} \partial_{TTTT}^4\right\} f_i = 0,$$

where $f_i = h_i Q_i$, $i = 1, 2, 3$, and the interfacial displacements for the long-wave component are related to the f_i by

$$Z_T = f_{1XX}, \quad N_T = -f_{3XX}. \tag{A 5}$$

Continuing the analysis to higher order, we expand the coefficient functions in the asymptotic sequence

$$\epsilon A_i = \epsilon A_i^{(0)} + \epsilon\mu A_i^{(1)} + \epsilon\mu\delta A_i^{(2)} + \epsilon\mu^2 A^{(3)}_i + \dots \tag{A 6}$$

(the required form for these expansions is evident from the dynamic boundary conditions, for example) and substituting these expressions into the boundary and matching conditions yields systems of *inhomogeneous* equations for $A_i^{(1)}$, $i = 1, 2, 3$, and

$h_iQ_i = f_i^{(1)}$. The equations for the $A_i^{(1)}$ are solvable only if the short wave evolves according to the equation

$$i\epsilon\mu(\zeta_T^{(1,0)} + C_g\zeta_X^{(1,0)}) + \epsilon\mu^2\frac{\omega''}{2}\zeta_{XX}^{(1,0)} = \epsilon\mu\delta\nu\zeta^{(1,0)}N^{(0)} + \dots. \tag{A 7}$$

The inhomogeneous long-wave conditions can be manipulated to yield the forced wave equation

$$\mathscr{L}_w N_T^{(1)} = \alpha(|\zeta^{(1,0)}|^2)_{XXXXX}, \tag{A 8}$$

where $\mathscr{L}_w$ is the fourth-order operator defined in (A 5).

The goal of the analysis is the computation of the coupling coefficients ν and α. After *extensive* algebraic manipulation, they are determined to be:

$$\begin{aligned}\nu = \frac{\omega k}{2(1-\mathscr{D}_{12})}\frac{T_2}{1-T_2}\frac{1}{\nu_D}\Big\{&\mathscr{F}_{12}(1-\mathscr{D}_{12})+\mathscr{F}_{23}(1-\mathscr{D}_{23})\\ &-\frac{\rho_1}{\rho_2}\mathscr{F}_{23}(1-\mathscr{D}_{23})\left[1-\frac{C_0/C(k)}{kh_1T_1}\right]-\frac{\rho_3}{\rho_2}\mathscr{F}_{12}(1-\mathscr{D}_{12})\left[1-\frac{C_0/C(k)}{kh_3T_3}\right]\\ &-\frac{C_0/C(k)}{kh_2T_2}(1-\mathscr{D}_{12})(1-\mathscr{D}_{23})[\mathscr{F}_{12}+\mathscr{F}_{23}-2(1-T_2)\mathscr{F}_{12}\mathscr{F}_{23}]\\ &+\frac{(1-\mathscr{D}_{23})}{T_2}\left[\frac{1+T_2}{T_2}\frac{2T_1+T_2}{T_1}-\frac{1-T_2^2}{T_2}\mathscr{F}_{12}-\frac{T_1+T_2}{T_1T_2}\mathscr{F}_{23}\right]\\ &+\frac{(1-\mathscr{D}_{12})}{T_2}\left[\frac{1+T_2}{T_2}\frac{2T_3+T_2}{T_3}-\frac{1-T_2^2}{T_2}\mathscr{F}_{23}-\frac{T_2+T_3}{T_2T_3}\mathscr{F}_{12}\right]\\ &+\frac{C_0/C(k)}{kh_1T_2}(1-\mathscr{D}_{23})\left[1+\frac{h_1}{h_2}(1-\mathscr{D}_{12})\right][(1+T_2)-\mathscr{F}_{23}]\\ &+\frac{C_0/C(k)}{kh_3T_2}(1-\mathscr{D}_{12})\left[1+\frac{h_3}{h_2}(1-\mathscr{D}_{23})\right][(1+T_2)-\mathscr{F}_{12}]\\ &+\frac{1-T_2}{T_1T_2T_3}\frac{\rho_3T_2+\rho_2T_3}{\rho_2T_3(1-T_2)}\frac{\rho_2T_1+\rho_1T_2}{\rho_2T_1(1-T_2)}\left[T_1\frac{\Omega_{23}^2}{\omega^2}\left(1-\frac{\Omega_{12}^2}{\omega^2}\right)(1-\mathscr{D}_{12})\left(1+\frac{C_0}{C(k)}\frac{T_3}{kh_3}\right)\right.\\ &\left.+T_3\frac{\Omega_{12}^2}{\omega^2}\left(1-\frac{\Omega_{23}^2}{\omega^2}\right)(1-\mathscr{D}_{23})\left(1+\frac{C_0}{C(k)}\frac{T_1}{kh_1}\right)\right]\Big\},\end{aligned} \tag{A 9}$$

where

$$\nu_D = \frac{\rho_2T_1+\rho_1T_2}{\rho_2T_1(1-T_2)}\frac{\rho_2T_3+\rho_3T_2}{\rho_2T_3(1-T_2)}\left[\frac{\Omega_{23}^2}{\omega^2}\left(1-\frac{\Omega_{12}^2}{\omega^2}\right)+\frac{\Omega_{12}^2}{\omega^2}\left(1-\frac{\Omega_{23}^2}{\omega^2}\right)\right];$$

and

$$\begin{aligned}\alpha = \omega^2h_2C_g^3\left(1-\frac{C_{12}^2}{C_0^2}\right)\left(1-\frac{C_{23}^2}{C_0^2}\right)&\left\{2\frac{\rho_2-\rho_1}{\rho_2}+\frac{\rho_1}{\rho_2}\frac{1+T_1^2}{T_1^2}-\frac{(1-T_2)^2}{2T_2^2}\right.\\ &\left.\times[\mathscr{F}_{12}^2(1-\mathscr{F}_{23})^2+(1-\mathscr{F}_{12})^2]+2\frac{C}{C_g}\frac{\Omega_{12}^2}{\omega^2}\frac{\rho_2T_1+\rho_1T_2}{\rho_2T_1^2T_2}\right\}\\ +\omega^2h_2C_g(C_g^2-C_{12}^2)\frac{\mathscr{F}_{12}}{\mathscr{F}_{23}}\frac{\rho_2h_3}{\rho_2h_3+\rho_3h_2}&\left\{2\frac{\rho_3-\rho_2}{\rho_2}-\frac{\rho_3}{\rho_2}\frac{1+T_3^2}{T_3}+\frac{(1-T_2)^2}{2T_2^2}\right.\\ &\left.\times[\mathscr{F}_{23}^2(1-\mathscr{F}_{12})^2+(1-\mathscr{F}_{23})^2]-2\frac{C}{C_g}\frac{\Omega_{23}^2}{\omega^2}\frac{\rho_2T_3+\rho_3T_2}{\rho_2T_3^2T_2}\right\}\end{aligned}$$

$$-\frac{2\omega C_g^2}{T_1T_2T_3\mathscr{F}_{23}}\frac{\rho_2h_3}{\rho_2h_3+\rho_3h_2}\left[\frac{\rho_2h_1}{\rho_2h_1+\rho_1h_2}C_g^2-(C_g^2-C_{12}^2)\right]\{\mathscr{F}_{12}T_1T_2+\mathscr{F}_{23}T_2T_3$$

$$+T_1T_3(\mathscr{F}_{12}+\mathscr{F}_{23})-2T_1T_3(1-T_2)\mathscr{F}_{12}\mathscr{F}_{23}\}$$

$$-\frac{2\omega}{T_3}\frac{\mathscr{F}_{12}}{\mathscr{F}_{23}}C_g^4\left[\left(1-\frac{C_{12}^2}{C_g^2}\right)\left(1-\frac{C_{23}^2}{C_g^2}\right)-\left(1-\frac{C_{12}^2}{C_0^2}\right)\left(1-\frac{C_{23}^2}{C_0^2}\right)\right],$$

where

$$\mathscr{F}_{12}=\frac{\rho_2T_1+\rho_1T_2}{\rho_2T_1(1-T_2)}\left(1-\frac{\Omega_{12}^2}{\omega^2}\right),\quad \mathscr{F}_{23}=\frac{\rho_2T_3+\rho_3T_2}{\rho_2T_3(1-T_2)}\left(1-\frac{\Omega_{23}^2}{\omega^2}\right),$$

$$\mathscr{D}_{12}=\frac{\rho_2h_1+\rho_1h_2}{\rho_2h_1}\left(1-\frac{C_{12}^2}{C_0^2}\right),\quad \mathscr{D}_{23}=\frac{\rho_3h_2+\rho_2h_3}{\rho_2h_3}\left(1-\frac{C_{23}^2}{C_0^2}\right),$$

and

$$C_{12}=\lim_{h_3\to0}C(k),\quad C_{23}=\lim_{h_1\to0}C(k),\quad C_0=\lim_{k\to0}C(k).$$

One non-trivial check on the accuracy of these coefficients is that they are unchanged with respect to an interchange of the subscripts 1 and 3. Another independent check on the long-wave coefficient α is that it reduces to the appropriate form for the forced long-wave component in the two-layer solution, when the limit $h_3 \to 0$ is applied.

The resonant condition is clarified by defining the new independent variables

$$\xi = X - C_gT,\quad \tau = \mu T.$$

Then, writing equations (A 7), (A 8) in terms of these variables and transforming back to the original variables, it is relatively simple to show that the resonant case with $C_g \approx C_0$ requires the scaling

$$\mu = \delta = \epsilon^{\frac{2}{3}}$$

and the resonant bandwidth is

$$\left|\frac{C_0-C_g(k)}{C_g(k)}\right| \leqslant O(\epsilon^{\frac{2}{3}}).$$

REFERENCES

Djordjevic, V. & Redekopp, L. 1977 On two dimensional packets of capillary–gravity waves. *J. Fluid Mech.* **79**, 703.

Fornberg, B. 1977 On a Fourier method for the integration of hyperbolic equations. *SIAM J. Numerical Analysis* **12**, 509.

Grimshaw, R. 1977 The modulation of an internal gravity wave packet, and the resonance with the mean motion. *Studies Appl. Math.* **56**, 241.

Hasimoto, H. & Ono, H. 1972 Nonlinear modulation of gravity waves. *J. Phys. Soc. Japan* **33**, 805.

Koop, C. G. 1981 Some observations of crosswave structure in an internal wave system. *Phys. Fluids* (submitted).

Koop, C. G. & Butler, G. 1981 An investigation of internal solitary waves in a two-fluid system. *J. Fluid Mech.* **112**, 225.

Koop, C. G., Rungaldier, H. & Sherman, J. 1979 An infrared optical sensor for measuring internal interfacial waves. *Rev. Sci. Instrum.* **50**, 20.

Lake, B. M., Yuen, H., Rungaldier, H. & Ferguson, W. 1977 Nonlinear deep water waves: theory and experiment. Part 2. Evolution of a continuous wavetrain. *J. Fluid Mech.* **83**, 49.

Lewis, J., Lake, B. M. & Ko, D. 1974 On the interaction of internal waves and surface gravity waves. *J. Fluid Mech.* **63**, 773.

McIntyre, M. 1973 Mean motions and impulse of a guided internal gravity wave packet. *J. Fluid Mech.* **60**, 801.

Ma, Y. C. & Redekopp, L. G. 1979 Some solutions pertaining to the resonant interaction of long and short waves. *Phys. Fluids* **22**, 1872.

Pinkel, R. 1975 Upper ocean internal wave observation from FLIP. *J. Geophys. Res.* **80**, 3892.

Yates, C. L. 1978 Internal wave generation by resonantly interacting surface waves. Ph.D. dissertation, The Johns Hopkins University.